Titania's radius and an upper limit on its atmosphere from the September 8, 2001 stellar occultation

T. Widemann [a,*], B. Sicardy [a,b], R. Dusser [c], C. Martinez [d], W. Beisker [e], E. Bredner [e], D. Dunham [f], P. Maley [g], E. Lellouch [a], J.-E. Arlot [h], J. Berthier [h], F. Colas [h], W.B. Hubbard [i], R. Hill [i], J. Lecacheux [a], J.-F. Lecampion [j], S. Pau [a], M. Rapaport [j], F. Roques [a], W. Thuillot [h], C.R. Hills [k], A.J. Elliott [l], R. Miles [l], T. Platt [m], C. Cremaschini [n], P. Dubreuil [o], C. Cavadore [p], C. Demeautis [p], P. Henriquet [q], O. Labrevoir [q], G. Rau [r], J.-F. Coliac [s], J. Piraux [t], Ch. Marlot [u], C. Marlot [u], F. Gorry [u], C. Sire [u], B. Bayle [v], E. Simian [w], A.M. Blommers [x], J. Fulgence [y], C. Leyrat [z], C. Sauzeaud [z], B. Stephanus [z], T. Rafaelli [aa], C. Buil [ab], R. Delmas [ab], V. Desnoux [ab], C. Jasinski [ab], A. Klotz [ab], D. Marchais [ab], M. Rieugnié [ac], G. Bouderand [ad], J.-P. Cazard [ad], C. Lambin [ad], P.-O. Pujat [ad], F. Schwartz [ad], P. Burlot [ae], P. Langlais [ae], S. Rivaud [ae], E. Brochard [af], Ph. Dupouy [ag], M. Lavayssière [ag], O. Chaptal [ah], K. Daiffallah [ai], C. Clarasso-Llauger [aj], J. Aloy Doménech [aj], M. Gabaldá-Sánchez [aj], X. Otazu-Porter [aj], D. Fernández [ak], E. Masana [ak], A. Ardanuy [al], R. Casas [al], J.A. Ros [al], F. Casarramona [al], C. Schnabel [al], A. Roca [al], C. Labordena [al], O. Canales-Moreno [c], V. Ferrer [am], L. Rivas [am], J.L. Ortiz [ap], J. Fernández-Arozena [aq], L.L. Martín-Rodríguez [aq], A. Cidadão [ar], P. Coelho [ar], P. Figueiredo [ar], R. Gonçalves [ar], C. Marciano [ar], R. Nunes [ar], P. Ré [ar], C. Saraiva [ar], F. Tonel [ar], J. Clérigo [as], C. Oliveira [as], C. Reis [as], B.M. Ewen-Smith [at], S. Ward [at], D. Ford [at], J. Gonçalves [au], J. Porto [au], J. Laurindo Sobrinho [an,av], F. Teodoro de Gois [ar], M. Joaquim [ao], J. Afonso da Silva Mendes [ao], E. van Ballegoij [x], R. Jones [aw], H. Callender [aw], W. Sutherland [aw], S. Bumgarner [f], M. Imbert [ax], B. Mitchell [ax], J. Lockhart [ax], W. Barrow [ax], D. Cornwall [ax], A. Arnal [ay], G. Eleizalde [ay], A. Valencia [ay], V. Ladino [az], T. Lizardo [az], C. Guillén [az], G. Sánchez [az], A. Peña [az], S. Radaelli [az], J. Santiago [az], K. Vieira [az], H. Mendt [ba], P. Rosenzweig [bb], O. Naranjo [bb], O. Contreras [bb], F. Díaz [bb], E. Guzmán [bb], F. Moreno [bb], L. Omar Porras [bb], E. Recalde [bd], M. Mascaró [bd], C. Birnbaum [bc], R. Cósias [bd], E. López [bd], E. Pallo [bd], R. Percz [bd], D. Pulupa [bd], X. Simbaña [bd], A. Yajamín [bd], P. Rodas [bd], H. Denzau [e], M. Kretlow [e], P. Valdés Sada [be], R. Hernández [be], A. Hernández [bf], B. Wilson [bg], E. Castro [bh], J.M. Winkel [x]

[a] Observatoire de Paris, LESIA, 5, Place Jules Janssen, 92195 Meudon cedex, France
[b] Université Pierre et Marie Curie et Institut Universitaire de France, 103 boulevard Saint-Michel, F-75005 Paris, France
[c] European Asteroidal Occultation Network (EAON), 60 impasse des Lauriers, F-84400 Apt, France
[d] Instituto Superior de Ciencias Astronómicas, and Liga Iberoamericana de Astronomía, Buenos Aires, Argentina
[e] International Occultation Timing Association, European Section (IOTA/ES), Bartold-Knaust-Strasse 8, 30459 Hannover, Germany
[f] International Occultation Timing Association (IOTA), PO Box 6356, Kent, WA 98064-6356, USA
[g] IOTA, 4535 Cedar Ridge Trail, Houston, TX 77059, USA
[h] Observatoire de Paris, IMCCE, 77 Avenue Denfert-Rochereau, 75014 Paris, France
[i] Lunar and Planetary Laboratory, University of Arizona, Tucson, AZ 85721, USA
[j] Observatoire de Bordeaux, 2, Rue de l'Observatoire, BP 89, 33270 Floirac, France
[k] Simoco Digital Systems Ltd, Radio House, St Andrews Road, Cambridge, Cambridgeshire, CB4 1GR, United Kingdom
[l] British Astronomical Association, Asteroids and Remote Planets Section, Lower Earley, Reading, RG6 4AZ, United Kingdom
[m] Starlight Xpress, Foxley Green Farm, Ascot Road, Holyport, Berkshire, SL6 3LA, United Kingdom
[n] Osservatorio di Trieste, Via G.B. Tiepolo 11, I-34143 Trieste, Italy
[o] Astrocam, F-06790 Aspremont, France
[p] Observatoire du Tim, Chemin La Chapelle, 04700 Puimichel, France
[q] Centre d'Astronomie, 04870 St.-Michel l'Observatoire, France
[r] Observatoire de Haute-Provence/CNRS, 04870 St.-Michel l'Observatoire, France
[s] Association Marseillaise d'Astronomie, 213, Avenue de Montolivet, F-13012 Marseille, France
[t] Laboratoire de Mécanique et d'Acoustique, UPR 7051, 31 chemin Joseph-Aiguier, F-13402 Marseille cedex 20, France
[u] ASCT Section Astronomie, 3 rue du 19 mars 1962, F-76400 Toussaint, France
[v] Home observatory, F-13300 Salon de Provence, France
[w] Astronomie en Crau, F-13310 Saint-Martin de Crau, France
[x] Dutch Occultation Association, Boerenweg 32, NL 5944 EK Arcen, The Netherlands
[y] Impasse de Biaune, F-21160 Corcelles les Monts, France
[z] Observatoire du Collège de l'Etang de l'Or, UAI 180, 34130 Mauguio, France
[aa] Observatoire de Malibert, F-34360 Saint-Chinian, France
[ab] Association des Utilisateurs de Détecteurs Electroniques (AUDE), c/o F. Colas, 45, Avenue Reille, 75014 Paris, France
[ac] Observatoire d'astronomie de Saint-Caprais, F-81800 Rabastens, France
[ad] Observatoire Jolimont, 1 Avenue Camille-Flammarion, 31500 Toulouse, France

[ae] *Société d'astronomie populaire poitevine (SAPP), Centre Socio culturel du Clos Gaultier, F-86000 Poitiers, France*

[af] *Observatoire de Saint-Savinien sur Charente, F- 17350 Saint-Savinien sur Charente, and Association Nationale pour la Protection du Ciel Nocturne (A.N.P.C.N), c/o S.A.F, 3 rue Beethoven, F-75016 Paris, France*

[ag] *Observatoire de Dax, rue Pascal Lafitte, F-40100 Dax, France*

[ah] *Centre de Documentation Spécialisé en Astronomie – CDSA Martinique, 34 Boulevard Amilcar Cabral, Cluny – BP 411, F-97200 Fort-de-France, France*

[ai] *Observatory of Algiers, CRAAG, Route de l'Observatoire, BP 63, Bouzaréah 16340, Algiers, Algeria*

[aj] *Agrupación Astronómica de Barcelona, Carrer Aragó 141-143, 2-E, 08015 Barcelona, Spain*

[ak] *Departamento de d'Astronomia i Meteorología, IEEC-Universitat de Barcelona, Avenue Diagonal 647, 08028 Barcelona, Spain*

[al] *Agrupación Astronómica de Sabadell, C. Prat de la Riba, s/n, Apdo 50, Sabadell, Barcelona, Spain*

[am] *Asociación Valenciana de Astronomía, 16 Bajo Valencia, 46014 Valencia, Spain*

[an] *Sociedade Portuguesa de Astronomia, Centro de Astrofísica da Universidade do Porto, Rua das Estrelas, 4150-762 Porto, Portugal*

[ao] *Associação de Astrónomos Amadores da Madeira (AAAM), Villas da Bela Vista, Moradia X, 9125-103 Caniço, Madeira, Portugal*

[ap] *Instituto de Astrofísica de Andalucía, Apdo. 3004, 18080 Granada, Spain*

[aq] *Agrupación Astronómica Isla de La Palma (AAP), Apartado de Correos 449, 38700 Santa Cruz de La Palma, Provincia de Santa Cruz de Tenerife, Islas Canarias, Spain*

[ar] *Associação Portuguesa de Astrónomos Amadores (APAA), Rua Alexandre Herculano 57-4° Dto, 1250-010 Lisboa, Portugal*

[as] *Associação Nacional de Observação Astronómica (ANOA), Apartado 582, 2430 Marinha Grande, Portugal*

[at] *Centro de Observação Astronómica no Algarve (COAA), Poio, 8500 Portimão, Portugal*

[au] *Núcleo Açoriano da Associação Portuguesa de Astrónomos Amadores (NAAPAA), Açores, Portugal*

[av] *Universidade da Madeira, Departamento de Matemática e Engenharias, Grupo de Astronomia, Campus da Penteada, 9000-390 Funchal, Madeira, Portugal*

[aw] *Barbados Astronomical Society, Harry Bayley Observatory, Bridgetown, St. Michael, Barbados*

[ax] *Trinidad & Tobago Astronomical Society, Sir Frank Stockdale Building, The University of the West Indies (UWI), St-Augustine Campus, Trinidad and Tobago*

[ay] *Observatorio Arval, Santa Teresa, Caracas, Venezuela*

[az] *Asociación Larense de Astronomía (ALDA), Barquisimeto, Lara, Venezuela*

[ba] *American Association of Variable Star Observers, 49 BayState Rd., Cambridge, MA 02138, USA*

[bb] *Universidad de Los Andes, Facultad de Ciencias, 5101, Mérida, Venezuela*

[bc] *Cité des Sciences et de l'Industrie, 30 avenue Corentin-Cariou, 75930 Paris cedex 19, France*

[bd] *Observatorio Astronómico de Quito, Parque de la Alameda, PO Box 17-01-165, Quito, Ecuador*

[be] *Universidad de Monterrey, Departamento de Física y Matemáticas, Avenue I. Morones Prieto, 4500 Pte., San Pedro Garza García, N.L. 66238, Mexico*

[bf] *Asociación Panamena de Aficionados de la Astronomía, Panama*

[bg] *George Observatory, Brazos Bend State Park, Houston, TX 77030, USA*

[bh] *Universidad Autónoma de Nuevo Leon, Facultad de Ciencias Físico Matemáticas, Avenue Universidad s/n, Ciudad Universitaria, San Nicolás de los Garza, N.L. 66451, Mexico*

A R T I C L E　I N F O

A B S T R A C T

On September 8, 2001 around 2 h UT, the largest uranian moon, Titania, occulted Hipparcos star 106829 (alias SAO 164538, a V = 7.2, K0 III star). This was the first-ever observed occultation by this satellite, a rare event as Titania subtends only 0.11 arcsec on the sky. The star's unusual brightness allowed many observers, both amateurs or professionals, to monitor this unique event, providing fifty-seven occultations chords over three continents, all reported here. Selecting the best 27 occultation chords, and assuming a circular limb, we derive Titania's radius: $R_T = 788.4 \pm 0.6$ km (1-σ error bar). This implies a density of $\rho = 1.711 \pm 0.005$ g cm^{-3} using the value $GM = (2.343 \pm 0.006) \times 10^{11}$ m^3 s^{-2} derived by Taylor [Taylor, D.B., 1998. Astron. Astrophys. 330, 362–374]. We do not detect any significant difference between equatorial and polar radii, in the limit $r_{eq} - r_{po} = -1.3 \pm 2.1$ km, in agreement with *Voyager* limb image retrieval during the 1986 flyby. Titania's offset with respect to the DE405 + URA027 (based on GUST86 theory) ephemeris is derived: $\Delta\alpha_T \cos(\delta_T) = -108 \pm 13$ mas and $\Delta\delta_T = -62 \pm 7$ mas (ICRF J2000.0 system). Most of this offset is attributable to a Uranus' barycentric offset with respect to DE405, that we estimate to be: $\Delta\alpha_U \cos(\delta_U) = -100 \pm 25$ mas and $\Delta\delta_U = -85 \pm 25$ mas at the moment of occultation. This offset is confirmed by another Titania stellar occultation observed on August 1st, 2003, which provides an offset of $\Delta\alpha_T \cos(\delta_T) = -127 \pm 20$ mas and $\Delta\delta_T = -97 \pm 13$ mas for the satellite. The combined ingress and egress data do not show any significant hint for atmospheric refraction, allowing us to set surface pressure limits at the level of 10–20 nbar. More specifically, we find an upper limit of 13 nbar (1-σ level) at 70 K and 17 nbar at 80 K, for a putative isothermal CO$_2$ atmosphere. We also provide an upper limit of 8 nbar for a possible CH$_4$ atmosphere, and 22 nbar for pure N$_2$, again at the 1-σ level. We finally constrain the stellar size using the time-resolved star disappearance and reappearance at ingress and egress. We find an angular diameter of 0.54 ± 0.03 mas (corresponding to 7.5 ± 0.4 km projected at Titania). With a distance of 170 ± 25 parsecs, this corresponds to a radius of 9.8 ± 0.2 solar radii for HIP 106829, typical of a K0 III giant.

1. Introduction

Among the various techniques used to probe the physical properties of distant objects in the Solar System, ground-based stellar occultations are especially powerful. They provide kilometric accuracies or better on sizes and shapes, and may reveal tenuous atmospheres down to a few tens of nbar, as stellar rays are differentially refracted by a possible rarefied gas near the surface. On September 8, 2001 the bright (V = 7.2) Hipparcos-catalog star HIP 106829—a K0 III giant—was occulted by Titania, the largest uranian satellite (Table 1), which angular diameter subtends 0.11 arcsec only on the sky. This rare event was independently predicted by Jean Meeus (Belgium) in 1999 and later by one of us (Claudio Martinez, Argentina) in 2001.

A great variety of observations were made using both small portable telescopes and larger, fixed instruments. The brightness of HIP 106829 allowed an exceptionally high number of observers to gather timings for the event, and light curves for some of them, using a wide variety of acquisition systems and timing tech-

* Corresponding author.

E-mail address: thomas.widemann@obspm.fr (T. Widemann).

Table 1
Various parameters adopted in this paper.

Titania physical properties	
Gravitational constant	$G = 6.67259 \times 10^{-11}$ m^3 kg^{-1} s^{-2}
Titania's mass[a]	$GM = (2.343 \pm 0.006) \times 10^{11}$ m^3 s^{-2}
Rotation period[a]	$P = 8.706$ days
Bond albedo[b]	$A_B = 0.15 \pm 0.02$
Stellar occultations geometry	
Sept. 8, 2001 02:00 UT	
Distance[c] (km)	2.8504×10^9 km
North pole position angle	$P = 260.4°$
Sub-observer latitude	$B = -24.17°$
Sub-observer longitude	$L = 343.5°$
Star position at epoch (ICRF)	$\alpha = 324.55817850° \pm 7.4$ mas
	$\delta = -14.90997417° \pm 5.7$ mas
Aug. 1, 2003 04:28 UT	
Distance (km)	2.8557×10^9 km
North pole position angle	$P = 257.6°$
Sub-observer latitude	$B = -15.67°$
Sub-observer longitude	$L = 164.3°$
Star position at epoch (ICRF)	$\alpha = 333.9773096° \pm 20$ mas
	$\delta = -11.6156551° \pm 13$ mas
Atmospheric refractivity modeling	
Carbon dioxide molecular mass	$\mu = 7.308 \times 10^{-26}$ kg
Carbon dioxide molecular refractivity[d]	$K_{CO_2} = 1.566 \times 10^{-23}$ cm^3 molecule^{-1}
Methane molecular mass	$\mu = 2.664 \times 10^{-26}$ kg
Methane molecular refractivity[d]	$K_{CH_4} = 1.549 \times 10^{-23}$ cm^3 molecule^{-1}
Nitrogen molecular mass	$\mu = 4.652 \times 10^{-26}$ kg
Nitrogen molecular refractivity[d]	$K_{N_2} = 1.023 \times 10^{-23} +$
	$(5.888 \times 10^{-26}/\lambda_{\mu m}^2)$ cm^3 molecule^{-1}

Note. Mass determination using fixed J_2 solution 4 from Taylor (1998).
[a] Taylor (1998).
[b] Buratti et al. (1990).
[c] Yields a scale of 13,819 km at Titania per arcsec on the sky.
[d] Washburn (1930).

Fig. 2. Enlargement of Fig. 1. Titania's shadow over Europe and Africa observing stations. Light gray star symbols (green in the online version) are for stations where observations were attempted and/or achieved. Filled star symbols (red in the online version) mark the subset of twenty-seven stations used for limb fitting (Section 5). See Table 2 for circumstances and timings, and Table 3 for limb fitting data.

Fig. 3. Same as Fig. 2, for Central and South America. See Table 2 for circumstances and timings, and Table 3 for limb fitting data.

niques; proper motion and parallax measurements in Hipparcos and Tycho-2 catalogs provided prediction of the stellar position in the International Celestial Reference System (ICRS) at the time of event. More than eighty reports from about seventy stations were gathered, spanning Western Europe, various islands in the Northern Atlantic ocean and Caribbean region, as well as several countries in North and South America (Figs. 1–3 and Table 2).

The main goals of the observations were to (i) determine Titania's radius and possible oblateness; (ii) determine Titania's offset with respect to the DE405 + URA027 ephemeris; (iii) to search for an atmosphere around Titania, or derive significant constraints (upper limits) on an atmosphere.

Another important and unique aspect of this observation is that our determination of Titania's radius can be compared to remote sensing observations by the *Voyager* spacecraft during its January 1986 flyby. It allows us to validate a ground-based method for which a sub-kilometric accuracy is usually claimed. We determine an upper limit for a pure CO_2 atmosphere, along with other possible gaseous constituents (CH_4 and N_2) on Titania.
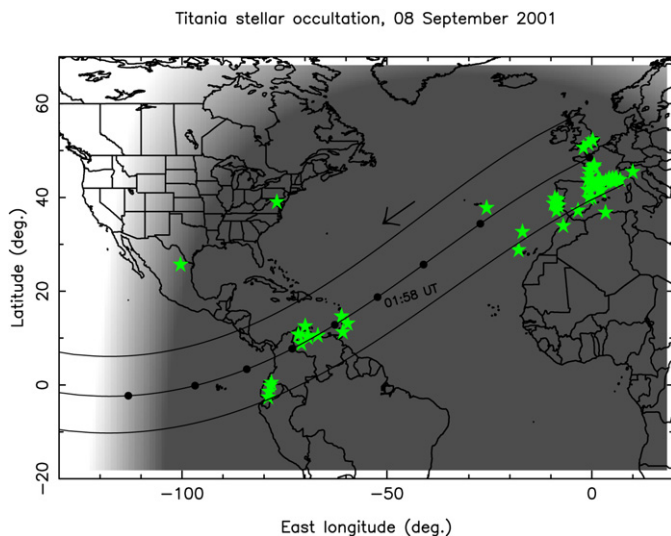

Fig. 1. Path of Titania's shadow on Earth on September 8, 2001, according to the post-occultation analysis presented in this paper. Motion is from upper right to lower left. The darker gray zone is for night time (Sun below $-18°$ with respect to local horizon), the gradually lighter gray is for astronomical twilight (Sun between $0°$ and $-18°$ below local horizon) and white is for day time. Dots along the centerline are plotted every minute. This is where the event duration was maximum, about 72 s. The white star symbols (green in the online version) indicate all the stations reported in Table 2, among which fifty-seven reported timings. The event was observed at low elevation from France, UK, Italy, Spain, Morocco, Portugal around 1:55 UT, and near zenith in the Caribbean region (Barbados, Tobago, Aruba) and from Northern South America (Ecuador, Venezuela) around 2:00 UT.
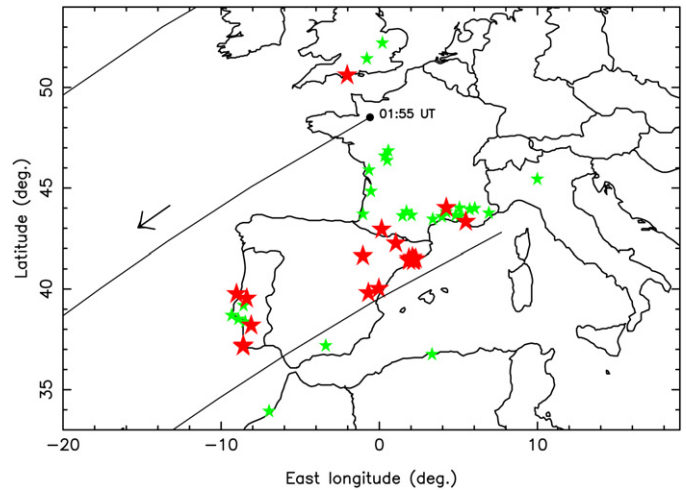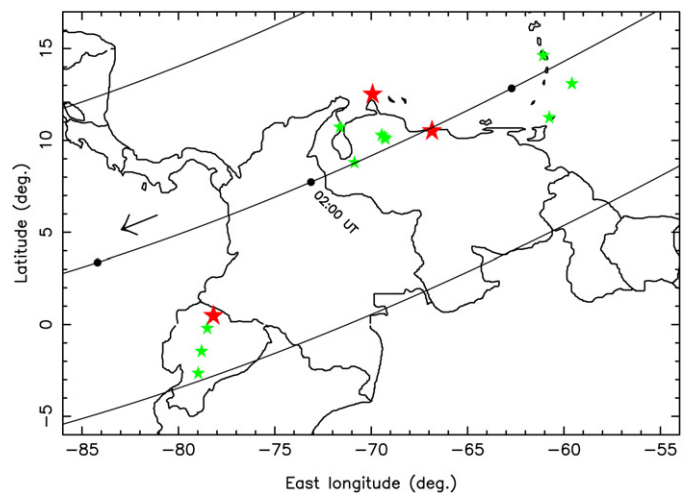
Table 2
Circumstances and timings of September 8, 2001 occultation of HIP 106829 by Titania, ordered by country of observing stations/datasets and event chronology from Northeast to Southwest.

Site name	Lat. (d:m:s), lon. (d:m:s), alt. (m)	Ingress UT, egress UT, cycle time	Telescope, instrument/receptor, timing ref. and remarks	Observers
		United Kingdom		
Teversham[b]	52:12:06 N 00:11:30 E 10 m	01:54:29.75 01:55:40-43.0 vis.	*R* 0.16 m Newt. Audio recording MSF and observer's commentary	C.R. Hills
Worth Hill Obs., Bournemouth[b,c,d]	50:35:52.9 N 02:01:50.5 W 140 m	01:54:29.08 ± 0.03 01:55:42.11 ± 0.03 0.04 s	*R* 0.25 m S/C Vid. DCF-77	A.J. Elliott
Binfield[b]	51:25:26 N 00:47:19.45 W 73 m	01:54:30 01:55:41 vis.	*r* 0.25 m Yolo off-axis timings Junghans "Mega" radio	R. Miles T. Platt
		Italy		
Pompiano, Brescia	45:26:14.2 N 09:59:30.3 E 94 m	Clouded out	*R* 0.2 m S/C n.a. n.a.	C. Cremaschini
		France		
Calern, Obs. Côte d'Azur[b,c]	43:44:54 N 06:55:36 E 1270 m	01:54:28 01:55:05 n.a.	*R* 0.2 m S/C Aud. CCD PC time from internet	P. Dubreuil
Puimichel[b,c]	43:58:53.1 N 06:02:10.0 E 680 m	01:54:19.7 ± 0.4 01:55:05.8 ± 0.4 n.a.	n.a. Audine, drift scan bad seeing (10")	C. Cavadore, C. Demeautis
Obs. Haute Provence[b,c]	43:55:46 N 05:42:45 E 650 m	01:54:21 01:55:07 0.04 s	*R* 0.8 m + *R* 0.6 m CCD & vid. SVHS recorder No data on *R* 0.6 m	W. Thuillot, P. Henriquet, O. Labrevoir, G. Rau
Marseille[b,c]	43:18:28 N 05:24:53 E 90 m	01:54:26 01:55:05 0.04 s	*R* 0.26 m, Newt. radio-piloted video and comments	J.F. Coliac
Les Orfeuilles, Marseille[b,c,d]	43:18:57 N 05:27:55 E 180 m	01:54:25.3 ± 0.2 01:55:03.5 ± 0.2 vis.	*R* 0.2 m S/C, micro-calculator HP71 calibrated with speaking clock and DCF 77	J. Piraux
Notre Dame de Lamaron, Plateau d'Albion[b]	44:00:11.2 N 05:04:05.4 E 1090 m	01:54:21.087 01:55:07.765 0.040 s	*R* 0.08 m Vid., digital camcorder Speaking clock, tape recorder, Stopwatch, beep every 10 s	F. Gorry, C. Marlot, Ch. Marlot, C. Sire
Salon[b,c]	43:36:00 N 05:06:00 E 40 m	01:54:25 01:55:09 0.04 s	*R* 0.2 m S/C Webcam Compro PS39 DCF77 timing	B. Bayle
St. Martin de Crau[b,c]	43:38:00 N 04:49:00 E 20 m	01:54:25 01:55:12 vis.	*R* 0.2 m S/C Radio clock, accuracy 1 s	E. Simian
St. Maurice de Cazevieille[b,c,d]	44:00:36 N 04:14:06 E 190 m	01:54:20.9 01:55:12.7 vis.	*R* 0.2 m S/C DCF77, stopwatch	A.M. Blommers
Nîmes[b]	43:48:05 N 04:14:05 E 170 m	01:54:22 01:55:18 vis.	R 0.114 m Newt. Speaking clock, stopwatch, tape recorder	J. Fulgence
Obs. de Mauguio[b,c]	43:34:07 N 03:57:07 E n.a.	01:54:180 01:55:070 0.015 sec	*R* 0.305 m S/C LX200 CCD KaF400 Time set on internet	C. Leyrat, C. Sauzeaud, B. Stephanus
Obs. Malibert, Pezenas[b,c]	43:26:48 N 03:22:46 E n.a.	01:54:28 01:55:17 vis.	*R* 0.15 m Mak-Cass. Speaking clock	T. Rafaelli
Guitalens[b]	43:38:34.7 N 02:02:11.2 E 148 m	01:54:22.6 01:55:18.9 n.a.	4 × *R* 0.2 m S/C, Four Audine cameras, drift scan DCF 77	C. Buil, R. Delmas, V. Desnoux, C. Jasinski, A. Klotz, D. Marchais

Table 2 (continued)

Site name	Lat. (d:m:s), lon. (d:m:s), alt. (m)	Ingress UT, egress UT, cycle time	Telescope, instrument/receptor, timing ref. and remarks	Observers
Rabastens	43:49:00 N 01:43:00 E (approx.)	duration 59 s vis.	r 0.4 m n.a.	M. Rieugnie
Obs. Jolimont Toulouse	43:36:43 N 01:27:46 E 189 m	n.a. 01:55:15 n.a.	n.a. Partly cloudy	G. Bouderand, J.-P.Cazard, C. Lambin, P.-O. Pujat, F. Schwartz
Chatellerault[b,c,d]	46:50:21.0 N 00:34:02.9 E 131 m	01:54:19.9 01:55:33.1 vis.	r 0.1 m, stopwatch DCF, synchro: Cuno inserter	E. Bredner
Poitiers	46:35:00 N 00:20:00 E (approx.)	No data	n.a.	J. Berthier
St. Maurice la Clouère[b]	46:22:00 N 00:30:00 E 120 m	$01:54:20.9 \pm 0.2$ $00:55:12.7 \pm 0.2$ vis.	R 0.12 m Newt.	P. Langlais, S. Rivaud, P. Burlot
St. Savinien sur Charente[b,c]	45:53:26.5 N 00:38:58.0 W 30 m	01:54:24.20 01:55:36.03 0.1 s	R 0.2 m S/C Aud. KAF 401E NTP server, poor absolute accuracy (several seconds)	E. Brochard
Bordeaux[b]	44:50:07 N 00:31:42 W 73 m	01:54:21 01:55:27 4.5 s	R 0.6 m, CCD camera	J.-F. Lecampion, M. Rapaport
Pic du Midi[b,c,d]	42:56:12 N 00:08:32 E 2870 m	$01:54:23.046 \pm 0.02$ $01:55:20.606 \pm 0.02$ 0.17 s	R 1.0 m, vid. & CCD (not used here) GPS timing	J. Lecacheux
Obs. de Dax[b]	43:41:36.4 N 01:01:49.8 W 11 m	Missed ingress 01:55:34.70 n.a.	R 0.32 m Newt. Aud. CCD DCF 77 timing	Ph. Dupouy, M. Lavayssière
Fort de France[b,c]	14:37:04 N 61:04:57 W n.a.	01:58:12.9 01:59:26.5 vis.	r 0.09 m	O. Chaptal
		Algeria		
Algiers	36:45:00 N 03:20:00 E 200 m	No event from 01:47 to 02:19, vis.	R 0.114 m Newt.	K. Daiffallah
		Morocco		
Les Sables d'Or Temara	33:55:07.4 N 06:58:08.6 W 6 m	No event for several mn around 01:55, vis.	R 0.06 m DCF 77 and short wave receptor, tape & stopwatch	R. Dusser
		Spain		
Alella[b,c,d]	41:29:02.3 N 02:18:01.8 E 45 m	$01:54:29.03 \pm 0.1$ $01:55:00.04 \pm 0.1$ 0.04 s	R 0.24 m S/C vid. + CCD, stopwatch, 10 MHz signals	C. Clarasso-Llauger
Barcelona-1[b,c,d]	41:25:18.9 N 02:12:10.0 E 60 m	$01:54:31.9 \pm 0.2$ $01:55:01.6 \pm 0.2$ vis.	R 0.258 m Dobson stopwatch DCF77	D. Fernández
Barcelona-2.1, L'Ordal[b,c,d]	41:23:32.4 N 01:52:48.0 E 540 m	$01:54:31.7 \pm 0.2$ $01:55:03.4 \pm 0.2$ vis.	R 0.21 m Newt. stopwatch, DCF77	J. Aloy-Doménech
Barcelona-2.2, L'Ordal[b,c,d]	41:23:32.4 N 01:52:48.0 E 540 m	$01:54:31.7 \pm 0.2$ $01:55:03.5 \pm 0.2$ vis.	R 0.203 m Newt. stopwatch + DCF77	M. Gabaldá-Sánchez
Barcelona-2.3, L'Ordal[b,c,d]	41:23:32.4 N 01:52:48.0 E 540 m	$01:54:31.5 \pm 0.2$ $01:55:03.3 \pm 0.2$ vis.	R 0.21 m Newt. stopwatch + DCF77	X. Otazu-Porter
Barcelona-3[b,c,d]	41:23:06.4 N 02:08:16.0 E 60 m	$01:54:32.2 \pm 0.2$ $01:55:02.0 \pm 0.2$ vis.	R 0.1 m Newt. stopwatch and radio signal	E. Masana
Esplugues de Llobregat[b]	41:22:38 N 02:05:37 E 120 m	n.a. 01:54:59.8	R 0.20 m CCD Cookbook, drift scan Manual set up of PC clock	F. Casarramona

Table 2 (*continued*)

Site name	Lat. (d:m:s), lon. (d:m:s), alt. (m)	Ingress UT, egress UT, cycle time	Telescope, instrument/receptor, timing ref. and remarks	Observers
St. Esteve Sesrovires[b,c,d]	41:29:41.5 N 01:52:25.7 E 180 m	$01:54:30.8 \pm 0.2$ $01:55:04.2 \pm 0.2$ vis.	*R* 0.2 m Newt. tape + DCF77	C. Schnabel
Obs. AAS Sabadell-1[b,c,d]	41:33:03 N 02:05:29 E 231 m	$01:54:30.865 \pm 0.1$ $01:55:03.825 \pm 0.1$ 0.25 s	*R* 0.5 m IOC, manual set up of PC clock	R. Casas, J.A. Ros
Obs. AAS Sabadell-2[b]	41:33:03 N 02:05:29 E 231 m	01:54:31.2 01:54:59.6 0.2 s	*R* 0.15 m Newt., webcam, manual set up of PC clock with time beeps	A. Ardanuy
Hortoneda[b,c,d]	42:14:49 N 01:02:35 E 1001 m	$01:54:23.2 \pm 0.2$ $01:55:11.0 \pm 0.2$ vis.	*R* 0.203 m Newt. stopwatch, time-signal from RNE1 station	A. Roca
Castellón[b,c,d]	40:00:31.5 N 00:01:48.2 W 85 m	$01:54:40.3 \pm 0.2$ $01:54:59.6 \pm 0.2$ vis.	*R* 0.2 m S/C and video, DCF77	C. Labordena
Zaragoza[b,c,d]	41:37:29.4 N 01:02:30.5 W 330 m	$01:54:27.6 \pm 0.2$ $01:55:18.7 \pm 0.2$ vis.	*R* 0.12 m Newt. stopwatch, time-signal from RNE1 station	O. Canales-Moreno
Cerro Los Molinos, Alcublas[b,c,d]	39:47:41 N 00:41:24 W 903 m	$01:54:39.9 \pm 0.2$ $01:55:01.5 \pm 0.2$ vis.	*R* 0.2 m Newt. stop watch and tape	L. Rivas, V. Ferrer
Granada	37:10:54 N 03:23:05 W n.a.	No event from 01:50:08 to 02:02:37	*R* 0.4 m and *R* 0.25 m CCD surveillance video camera	J.L. Ortiz
Roque de los Muchachos, Canaries Island	28:45:44 N 17:52:42 W 2333 m	No event from 1:52 to 2:03, vis.	*R* 0.125 m Newt., *R* 0.2 m S/C and *R* 0.25 m	J. Fernández-Arozena, L.L. Martín-Rodríguez
		Portugal		
Linhaceira, Tomar[b,c,d]	39:31:22.6 N 08:23:01.5 W 90 m	$01:54:36.35 \pm 0.02$ $01:55:37.39 \pm 0.02$ 0.04 s	*R* 0.25 m Newt. low-light vid. with AGC, VHS, DCF 77	R. Gonçalves
Almeirim[b]	39:10:50 N 08:34:58 W 10 m	01:54 37.7 01:55:34.0 0.04 s	*R* 0.25 m Webcam + PC Antennal timing	C. Reis
Marinha Grande[b,c,d]	39:45:00 N 09:01:58.8 W 30 m	$01:54:36.98 \pm 0.5$ $01:55:41.31 \pm 0.5$ 0.04 s	*R* 0.4 m S/C vid. timing from internet	J. Clérigo
Alvito[b,c,d]	38:11:01.8 N 08:06:11.0 W 50 m	$01:54:40.0 \pm 0.08$ $01:55:30.8 \pm 0.08$ 0.04 s	*R* 0.25 m S/C, vid., PAL system, PC Compaq 10 MHz times signal	C. Oliveira
Alcácer do Sal[b,c]	38:21:38.9 N 08:28:33 W 25 m	01:54:41 01:55:34 vis.	*R* 0.2 m S/C, stopwatch timing origin n.a.	C. Marciano
Setúbal[b,c]	38:30 N 08:55 W 40 m	01:54:36.5 01:55:33.0 1/15 s	*R* 0.25 m S/C, CCD, timing origin n.a.	R. Nunes, P. Coelho
Carcavelos[b,c]	38:41:11.4 N 09:20:44.5 W 56 m	01:54:42 01:55:41 0.1 s	*R* 0.25 m S/C, CCD, GPS	C. Saraiva, P. Figueiredo
Oeiras[b,c]	38:41:07 N 09:19:25 W 50 m	01:54:36 01:55:34 1/3.325 s	*R* 0.25 m SC, SBIG's ST-237 cooled CCD	A. Cidadão
Portimão-1[a,b,c,d] *0.25 m*	37:08:28.7 N 08:37:33.2 W 64 m	$01:54:45.611 \pm 0.035$ $01:55:27.831 \pm 0.035$ ± 0.27 s (fitted)	*R* 0.25 m S/C IOC, TC 245 chip DCF 77	H. Denzau, P. Ré, F. Tonel
COAA Algarve,[b,c,d] *Portimão-2*	37:11:24.6 N 08:36:01.8 W 65 m	$01:54:44.84 \pm 0.06$ $01:55:27.72 \pm 0.06$ 1/14.995 s	*R* 0.2 m Newt. low-light vid., AVI 60 kHz timing, soundtrack	B.M. Ewen-Smith, S. Ward, D. Ford
Espada Station, Funchal, Madeira	32:38:15.3 N 16:56:07.8 W 35 m	Clouded out	*R* 0.35 m S/C	R. Hill, W.B. Hubbard, J. Laurindo Sobrinho, F. Teodoro de Gois, J. Afonso da Silva Mendes, M. Joaquim

Table 2 (*continued*)

Site name	Lat. (d:m:s), lon. (d:m:s), alt. (m)	Ingress UT, egress UT, cycle time	Telescope, instrument/receptor, timing ref. and remarks	Observers
Ponta Delgada, Açores[b,c,d]	37:44:38 N 25:40:38 W 50 m	01:55:18.25 ± 0.30 01:56:31.15 ± 0.30 0.04 s	*R* 0.3 m S/C vid. & PC, DCF 77	J. Gonçalves, J. Porto
		United States of America		
Greenbelt, Maryland	38:59:10.1 N 76:52:09.9 W 53 m	No event	*R* 0.2 m S/C vid.	D. Dunham
		Aruba		
Arikok[a,b,c,d] 0.20 m	12:29:55.6 N 69:55:34.1 W 99 m	01:58:59.140 ± 0.005 02:00:08.680 ± 0.005 ±0.110 s (fitted)	*R* 0.2 m S/C IOC, TC245 chip GPS time	T. Widemann
Wela[b]	12:29:00.5 N 69:57:49.6 W 30 m	01:59:00.1 02:00:11.3 vis.	*R* 0.318 m Dobson Colorado time-signal station 15 MHz, stopwatch, cassette recorder	E. van Ballegoij
		Barbados		
Bridgetown[b]	13:05:07 N 59:35:10 W 74 m	01:58:14.4 01:59:22.9 vis.	*R* 0.35 m S/C, WWV time signal radio station, tape recorder	R. Jones, H. Callender, W. Sutherland
		Trinidad and Tobago		
Santa Margarita, Trinidad	n.a. n.a. n.a.	Clouded out	*R* 0.2 m S/C CCD	S. Bumgarner
Arnosvale, Tobago	11:13:54 N 60:45:42 W 100 m	Duration: 70.9 s	*R* 0.3 m S/C, CCD w/increased gain, Trinidad and Tobago Astron. Society's VHS video recorder	M. Imbert, B. Mitchell, J. Lockhart, W. Barrow, D. Cornwall
		Venezuela		
Obs. ARVAL, Caracas[b,c,d]	10:30:08.6 N 66:50:39.4 W 915 m	01:58:50.00 ± 0.05 02:00:04.73 ± 0.05 1/30 s	*R* 0.125 m S/C, PC23C, camera VHS tape (SP speed)	A. Arnal, G. Eleizalde, A. Valencia
Casetejas	10:04:44.91 N 69:14:54.86 W 465 m	Clouded out	n.a.	A. Peña, S. Radaelli
Tamaca	10:09:43.25 N 69:19:02.88 W 595 m	Clouded out	n.a.	J. Santiago, K. Vieira
Bobares 1[b,c]	10:16:19.5 N 69:27:20.52 W 620 m	01:59:00.25 02:00:13.50 vis.	*R* 0.275 m S/C	V. Ladino, T. Lizardo, P. Maley
Bobares 2	10:16:37.43 N 69:27:18 W 640 m	Clouded out	n.a.	C. Guillén, G. Sánchez
Maracaibo, Zulia[b]	10:42:53 N 71:37:25 W n.a.	About 01:59:00 About 02:00:00 vis.	*r* 0.05 m	H. Mendt
Mérida	08:47:00 N 70:52:00 W 3600 m	Clouded out	*R* 0.6 m IOC TC245 chip + *R* 1.0 m, video	O. Contreras, F. Díaz, E. Guzmán, M. Kretlow, F. Moreno, O. Naranjo, L. Omar Porras, P. Rosenzweig
		Ecuador		
Salinas 1[a,b,c,d] 0.25 m	00:28:01.5 N 78:11:06.6 W 2040 m	02:00:11.341 ± 0.01 02:01:11.166 ± 0.01 ±0.26 s (fitted)	*R* 0.25 m S/C IOC, TC245 chip GPS time	B. Sicardy, E. Recalde
Salinas 2[a,b,c,d] 0.20 m	00:28:01.5 N 78:11:06.6 W 2040 m	02:00:11.290 ± 0.02 02:01:11.120 ± 0.02 ±0.22 s (fitted)	*R* 0.2 m S/C IOC, TC245 chip GPS time	W. Beisker, M. Mascaró

Table 2 (*continued*)

Site name	Lat. (d:m:s), lon. (d:m:s), alt. (m)	Ingress UT, egress UT, cycle time	Telescope, instrument/receptor, timing ref. and remarks	Observers
Salinas-3	00:28:01.5 N 78:11:06.6 W 2040 m	02:00:12.150 02:01:10.185 ±0.100 s	*R* 0.2 m S/C Audine camera drift scan, manual time setup	C. Birnbaum, F. Colas, S. Pau
Quito	00:12:54.4 S 78:30:09.6 W 2818 m	Clouded out	*r* 0.238 m Mertz webcam	R. Cósias, E. López, E. Pallo, R. Percz, D. Pulupa, X. Simbaña, A. Yajamín
Cerro El Buerán, Cuenca[b]	02:39:46.3 S 78:58:24.2 W 3987 m	02:00:17.4 02:01:36.9 vis.	*r* 0.1 m	P. Rodas
Mexico				
Monterrey	25:38:36 N 100:22:26 W 659 m	No event from 01:51 to 02:05	*R* 0.175 m Astrovid camera	P. Valdés Sada

Note. Abbreviations and acronyms: Cycle time = Recording time resolution; Telescope: *R* = reflector; *r* = refractor; Newt. = Newton; S/C = Schmidt–Cassegrain; Instrument/Receptor: IOC = Iota camera, Aud. = Audine camera, SBIG = Sbig camera, Vid. = video/camcorder, Vis. = Visual; Timing source/reference: MSF (or NPL) = UK 60 kHz time signal, DCF77 = Germany 77.5 kHz time signal, WWVB = NIST 60 kHz time signal, Colorado; n.a. = not available/specified.

[a] The four stations/datasets used for stellar diameter (Section 3) and atmospheric model fitting (Section 6). Quoted error bars are formal errors from diffraction limb fitting and are at most 0.035 s. Larger, systematic errors on absolute timing may be present at the ±0.3 s level (see text).

[b] The fifty-seven stations with reported timings (shown in Fig. 7). Error bars at these stations are those reported by observers and have not been modified by us.

[c] The forty-three stations with $\Delta r = r_{i,\text{obs}} - r_{\text{ref}} \leqslant 10$ km used for Titania's ephemeris offset using time-shifted chords (Section 4 and Fig. 8).

[d] The twenty-seven stations used for Titania's size and oblateness through limb fitting (Section 5, fit parameters listed in Table 3). Among them are thirteen visual observations made by experienced observers, for which we estimate an accuracy of about 0.2–0.3 s.

We finally address the ability of the occultation technique to probe tenuous atmospheres down to the ∼10 nb level or below in distant Solar System objects. As pressure levels detected during refractive occultations are inversely proportional to distances, we discuss how this method would quantitatively apply to the detection and characterization of atmospheres of trans-neptunian objects at a few nanobar levels.

After a presentation and discussion of observing and timing techniques and limitations (Section 2), we derive the stellar diameter in Section 3, as a few stations could record individual images of the star as it disappeared (ingress) and reappeared (egress) from behind Titania's limb. Titania's offset with respect to the DE405 + URA027 ephemeris is given in Section 4. Titania' size and an upper limit for its oblateness is provided in Section 5. Upper limits for various types of atmospheres are given in Section 6, before concluding remarks in Section 7.

2. Occultation chords

2.1. Circumstances of the event

The observation of this occultation was attempted from more than seventy ground-based stations, totalizing more than eighty reports (Table 2). Note that not all stations actually recorded the event, due to weather conditions, technical problems, or being out of the shadow path. Fig. 1 shows a post-event reconstruction of Titania's shadow trajectory on Earth. Titania's shadow was cast on Earth's night side at a velocity of 20.92 km s^{-1} in the plane of the sky, yielding for a maximum possible duration about 75 s. The shadow first swept at low elevation over densely populated areas of Western Europe: France, UK, Italy, Portugal, Spain, and Portugal/Madeira; Northern Africa: Morocco, Algeria, and Spain/Canary Islands (Fig. 2). It was then visible at high elevation from the Caribbean: Aruba, Barbados, France/Martinique, Trinidad and Tobago, and finally South America: Ecuador, Venezuela, while being attempted from North America: Mexico and USA (Fig. 3). The Moon was not visible in the sky at that moment, thus causing no interference with observations.

Among the 70 or so observing stations, nine were clouded out: Quito (Ecuador), Pompiano (Italy), Madeira and Funchal (Portugal), Santa Margarita (Trinidad), Mérida and other three amateur stations in Venezuela. Six were outside the shadow: Algiers (Algeria), Monterrey (Mexico), Greenbelt (USA), Temara (Morocco), Granada and Canary Islands (Spain) see Table 2.

Among all stations, the highest elevation recording was at Cerro El Bueran near Cuenca (Ecuador) at 3987 m altitude, followed by Llano del Hato (Mérida, Venezuela) at 3600 m, and Pic du Midi (France), at 2878 m. Lowest elevation was sea level. The largest telescope were Pic-du-Midi (France) 1.05 m, followed by Observatoire de Haute-Provence (France) 1 m and 0.8 m, Mérida (Venezuela) 0.6 m which was clouded out, and Sabadell-1 (Spain) 0.5 m, while the Granada (Spain) 0.4 m telescope was outside the shadow. A historical refractor telescope built in 1873, the 23.8 cm Mertz refractor in downtown Quito (Ecuador) was also set up for this observation, but was unfortunately clouded out.

2.2. Recording modes

A wide range of telescope diameters has been used from 1.05 m (France/Pic-du-Midi) to a mere 5 cm (Venezuela/Maracaibo), as well as a large variety of camera devices, acquisition and timing methods, including visual and audio. Only a selection of observations turned out to be relevant for astrometry and limb fitting measurements, among which an even smaller selection consisted in extended lightcurves. A reliable method to constrain astrometry and limb shape of the occulting body is to combine frame by frame analysis and absolute timing capability. Frame by frame acquisition are provided by low-noise CCD cameras from various groups or vendors, such as IOC cameras by IOTA (International Occultation and Timing Association), Audine-series cameras by AUDE (Association des Utilisateurs de Détecteurs Electroniques), ST-series cameras by SBIG (Santa Barbara Instrument Group), among others, and in some cases, analog video tapes (Table 2).

The timing methods were either GPS-based, internet/internal PC clock, visual or audio (about 25 stations) consisting in either

stopwatch visual synchronization to a radio signal (DCF-77 or local/national radio), or audio recording of time signal or beeps, on the acquisition VHS tape or a separate audio recorder with observer's commentary. Absolute timing must be provided by a Global Positioning System (GPS), or an NTP server (Matsuda, 1996), directly connected to the file acquisition/recording device or to the PC clock time. Direct reading from the internet, without such precautions, should be avoided even for relative time measurements. Table 2 provides ingress and egress times, the observer's position in terrestrial coordinates, telescope diameter, acquisition instrument, visual recording and timing methods for each individual station.

3. Star properties

To reconstruct the geometry of the event we need (1) the position of the star at epoch, (2) Titania's ephemeris, (3) the observers' geocentric coordinates and (4) the timings of the occultation (star ingress and egress) at each station. These timings allow us to reconstruct the 2-D geometry of the stellar occultation by Titania's disk in the sky plane, and provide the offset between Titania's actual position and its calculated ephemeris.

3.1. Star position

The ICRS position for star HIP 106829 is provided by the Vizier site (Ochsenbein et al., 2000). This star is not documented as either variable nor multiple in the Hipparcos catalog. Its ICRS position at Hipparcos epoch (1991.25) is $\alpha = 324.55809702°$, $\delta = -14.91006013°$ with error of 0.8 and 0.6 milli-arcsec (mas), respectively. The Hipparcos catalog provides a proper motion of $\mu_\alpha \cos(\delta) = 27.703 \pm 1.314$ mas year^{-1} and $\mu_\delta = 29.5 \pm 0.72$ mas year^{-1}, while the Tycho 2 catalog gives $\mu_\alpha \cos(\delta) = 28.251 \pm 0.827$ mas year^{-1} and $\mu_\delta = 29.5 \pm 0.8$ mas year^{-1}. Weighing those proper motions according to errors, we obtain a total motion of $\Delta\alpha \cos(\delta)_{pm} = 295.516 \pm 7.368$ mas and $\Delta\delta_{pm} = 310.290 \pm 5.629$ mas between the Hipparcos epoch and the date of occultation (2001.7683).

The annual parallax of the star, from Hipparcos, is $\pi'' = 5.89 \pm 0.91$ mas (Perryman et al., 1997). This yields a further correction of $\Delta\alpha \cos(\delta)_{par} = -2.294 \pm 0.354$ mas and $\Delta\delta_{par} = -0.838 \pm 0.130$ mas, and finally:

$$\begin{cases} \alpha = 324.55817850° \pm [\Delta\alpha \cos(\delta) = 7.4 \text{ mas}], \\ \delta = -14.90997417° \pm [\Delta\delta = 5.7 \text{ mas}], \end{cases} \quad (1)$$

where the uncertainties essentially come from the propagation of the proper motion error between 1991.25 and 2001. At the distance of Titania, $D = 2.8504 \times 10^9$ km (Table 1), one arcsec corresponds to 13,819 km. Thus, the error bars quoted above correspond to distances of ~100 km in the plane of the sky.

3.2. Stellar diameter

A few stations could record individual images of the star as it disappeared (ingress) and reappeared (egress) from behind Titania's limb. We have selected the four best light curves in terms of timing accuracy, namely Salinas-1 (0.25 m) and Salinas-2 (0.20 m) in Ecuador, Arikok in Aruba island (0.20 m), and Portimão-1 in Portugal (0.25 m). All four datasets were collected with IOC cameras. An example of lightcurve, obtained with the 25-cm reflector at Salinas-1, is displayed in Fig. 4.

Individual fits to each gradual decrease and increase in star intensity have been performed for each of those experiments, providing eight timings (Table 2). Those times correspond to the instant when the center of the stellar disk intersects Titania' limb. Prior to the fit, the data were normalized between zero (Titania'
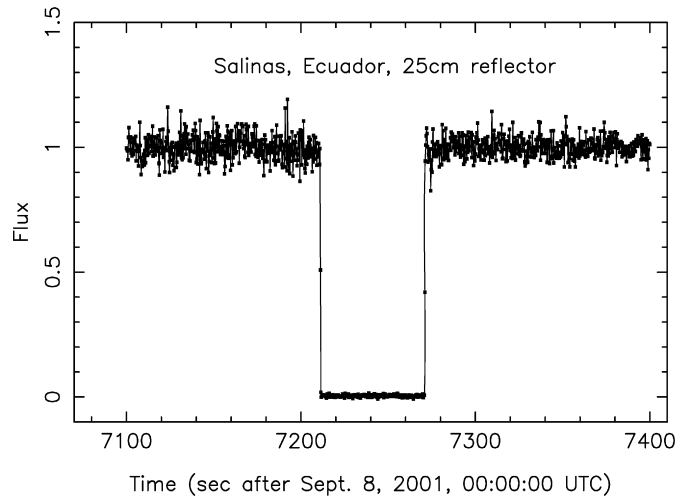

Fig. 4. Example of a light curve, obtained with the 0.25 m reflector at Salinas. All data points are shown, with a cycle time of 0.26 s, see Table 2. The flux from the star (plus the much fainter Titania) has been divided by a running average (over 5 s) of Uranus' flux, in order to correct for low frequency sky transparency variations. Finally, the data have been normalized between zero (Titania only) and unity (full stellar + Titania flux).
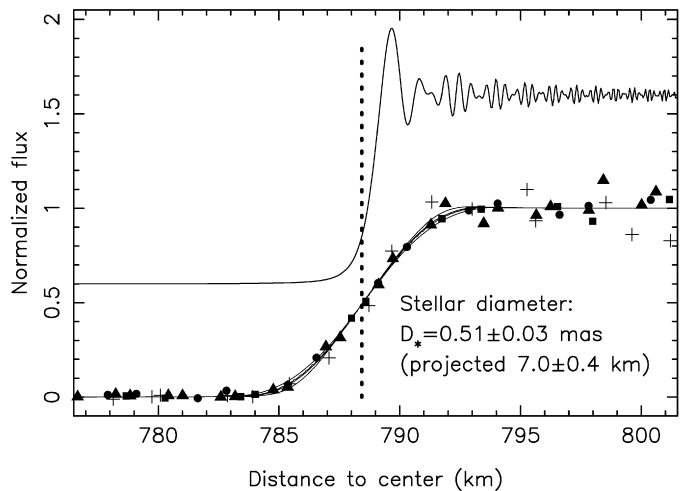

Fig. 5. Fit the stellar diameter from the Salinas-1 0.25 m (squares), Salinas-2 0.20 m (bullets), Arikok 0.20 m (triangles) and Portimão-1 0.25 m (crosses) light curves (see Table 2). Data are normalized between 0 (no star) and 1 (full signal). The vertical dotted line is the location of an edge at 788.4 km, corresponding to the Titania radius obtained in this paper. The upper thin curve is shifted vertically by +0.6 for better viewing, and shows the expected diffraction pattern from a point-like source. Thin lines superimposed to the data are best fits with stellar diameter taken into account. They are slightly different from each other, as the response of each instrument varies with integration time. See text for details.

flux only) and unity (flux of Titania plus star outside occultation). The fits include the following steps: (1) Fresnel diffraction by a point-like source at distance $D = 2.8504 \times 10^9$ km from the observer are generated. The numerical scheme used to generate this diffraction pattern is described in details in Roques et al. (1987). Because the IOC's were used in clear (no filter) mode, convolution with the camera bandwidth were performed. The resulting diffraction pattern is shown in Fig. 5, see the thin upper curve; (2) this profile was convolved by a 2-D stellar disk, taking into account limb darkening. The limb darkening profile was taken from Claret (2000), who provides a four-parameter model for the stellar disk specific intensity I: $I(\mu) = 1 - \sum_{k=1}^{4} a_k(1 - \mu^{k/2})$, where $\mu = \cos(\gamma)$, and γ is the angle between the line of sight and the intensity emerging from the stellar surface. Note that the in-
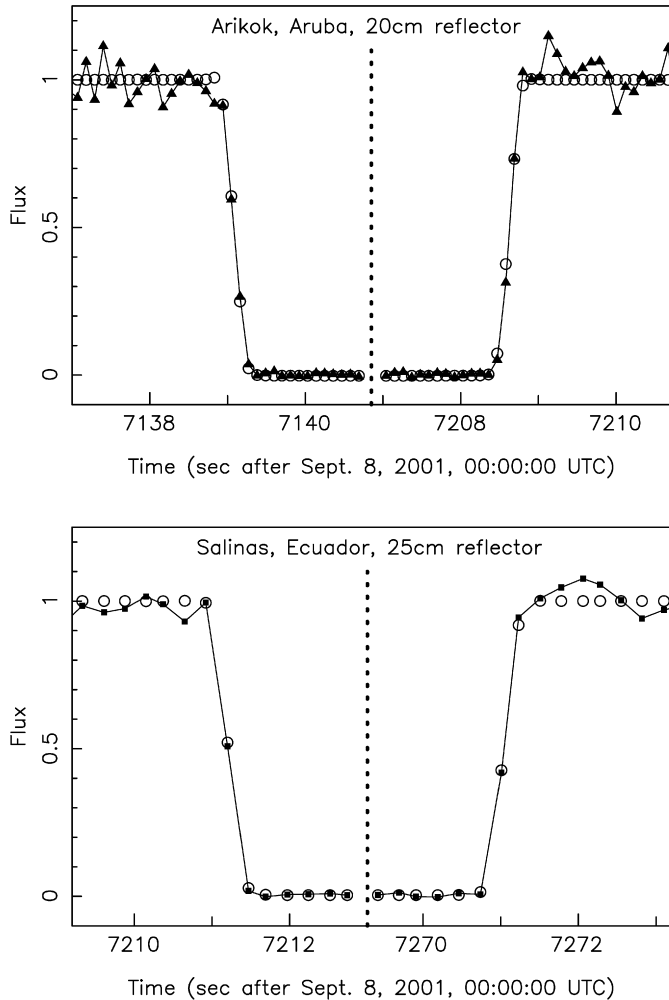
Fig. 6. *Upper panel*: Fit to the Arikok, Aruba, ingress and egress light curves (solid line). The triangles are the individual data points, while the open circles are from a best fit model, taking into account diffraction, stellar diameter and instrumental response, see text for details. Besides providing the stellar diameter, see Fig. 5, the fit yields the stellar half-light times at disappearance and reappearance, and associated error bars, see Table 2. *Lower panel*: The same for the Salinas-1 0.25 m reflector data, where the square are individual data points, see also Fig. 4. On both plots, note the discontinuity in time at the vertical dotted line, in order for the light curves to fit into the figure. Also, note the better sampling of the Arikok light curve, due to a smaller cycle time (0.11 s vs 0.26 s, see Table 2).

tensity is arbitrarily normalized to unity for $\mu = 1$. For a K0 giant star (effective temperature $T_{eff} = 4750$ K), this author gives: $a_{1,2,3,4} = 0.6699, -0.7671, 1.6405, -0.6607$, respectively; (3) a final convolution accounts for the instrumental response, namely the fact that each data point actually represents the number of photons received during a finite time step Δt. Examples of such fits to the Salinas-1, Salinas-2 and Arikok lightcurves are shown in Fig. 6.

The ingress/egress timings are derived from the classical minimization of:

$$\chi^2 = \sum \frac{(\Phi_{i,obs} - \Phi_{i,cal})^2}{\sigma_i^2}, \tag{2}$$

where Φ is the flux, "i" refers to the ith data point, "obs" refers to observations, "cal" refers to calculated, and σ_i is the expected 1-σ error of the ith data point. The latter is estimated from the signal fluctuations observed during a typical time interval of 2 mn around the event. Quoted formal errors on timings correspond to an increase of $\Delta \chi^2 = \chi^2 - \chi^2_{min} = 1$ with respect to the best obtained value, χ^2_{min}, the so-called 1-σ level, or more precisely, the 68.3% confidence level (Press et al., 1986).

In order to derive the stellar size, we need to align all the eight profiles along a common radial scale. To do so, we force the extremities of the four chords to lie on a common circle, with a reference radius $R_{T,occ} = 788.4$ km corresponding to Titania's best fit value later determined in Section 5. This reference radius is arbitrary since small timing errors and/or topographic features along Titania's limb may induce radial scatter at the km-level. This procedure is valid, however, as long as we are interested in the local behavior of the light curve during ingress and egress of the star.

Fig. 5 shows the data points plotted versus distance to Titania's shadow center. As noted before, the thin upper line shows the diffraction profile expected from a point-like star (but after convolution by the receptor bandwidth). Note that the main fringe has a width at half maximum of about 1 km. This is expected from the classical expression of the Fresnel scale, $L_F = \sqrt{\lambda D/2}$, where λ is the wavelength of observation and D is the distance to Titania. Thus, L_F varies from 0.9 to 1.1 km when λ varies from 0.6 to 0.9 μm (the typical coverage of IOC cameras), yielding the kilometric scale quoted above.

A χ^2 minimization similar to that of Eq. (1) provides the best fit stellar diameter projected at Titania, $D_\star = 7.5 \pm 0.4$ km, corresponding to an angular diameter of 0.54 ± 0.03 mas. The quoted error bar corresponds again to a variation $\Delta \chi^2 = 1$ above the best fit.

Thus, the occultation pattern is dominated by stellar diameter, not by diffraction. Note, however that the formal error bars on ingress/egress times are of the order of 0.010–0.035 s, corresponding to radial errors of 0.1–0.7 km depending on the star velocity perpendicular to Titania's limb. Thus, and at least for stations where individual images are available, sub-km radial errors can be achieved.

The stellar diameter obtained here can be compared to independent estimations, e.g. using the formulae of van Belle (1999). The magnitudes provided by the Simbad astronomical database (Wenger et al., 2000) are $m_B = 8.24$, $m_V = 7.20$, $m_J = 5.45$, $m_H = 4.90$, $m_K = 4.75$, from which we get an angular diameter of 0.59 mas, with typical errors of 10–20%. This is compatible with our determination, although with a larger error bar. The annual parallax of the star is 5.89 ± 0.91 mas (Perryman et al., 1997), corresponding to a distance of 170 ± 25 parsecs. Hence, our determination of the angular diameter yields a stellar radius of 9.8 ± 0.2 solar radii, where most of the error bars comes from the error on the annual parallax. This radius is typical of a K0 III giant star, for which $\log R/R_\odot = +1.2$ (Allen, 1976).

4. Titania's ephemeris offset

4.1. The September 8, 2001 occultation event

We first determine Titania's predicted position for the September 8, 2001 event with Horizons ephemeris provided by NASA's Jet Propulsion Laboratory (Giorgini et al., 1996). The on-line ephemeris is a combination of the DE405 motion of Uranus, and the URA027 satellite analytical ephemeris derived from the GUST86 theory (Laskar and Jacobson, 1987). As indicated in Table 1, it provides (i) the latitude of sub-Earth point at 02:00 UT (8 September 2001), $B = -24.2°$ (IAU convention), (ii) Titania's north pole position angle, $P = 260.4°$, with respect to the local J2000.0 celestial North, and (iii) the longitude of sub-Earth point, 343.5° (Earth and the Sun being about 1.2° apart as seen from Uranus). This allows us to reconstruct Titania's orientation in the sky plane, identify the meridian facing Uranus, as shown in Fig. 7, and associate a *titaniacentric* latitude to each ingress and egress occultation point, see Table 3. Note that the sub-occultation points provided in Table 3 represent a *subset* of the full dataset, as explained below.
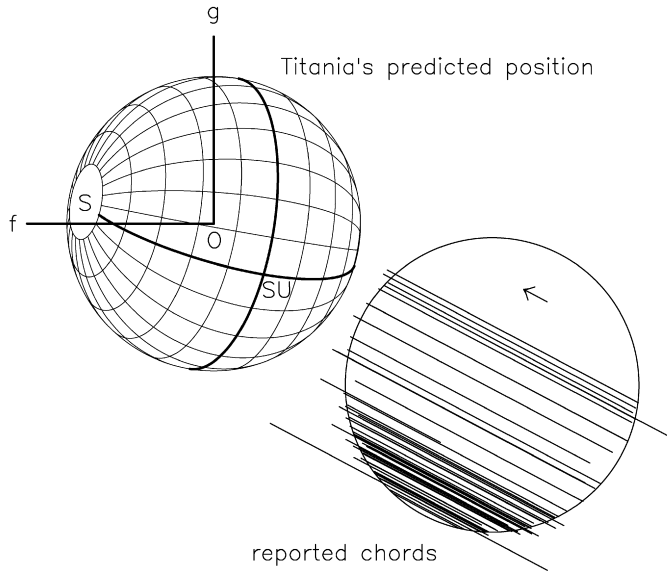
g

Titania's predicted position

f

S

O

SU

reported chords

Fig. 7. Fifty-seven occultation chords with reported timings (Table 2). The origin "O" of the diagram is located at the expected center of Titania's disk in ICRS J2000.0 coordinates, as derived from the star position predicted at time of event (Eq. (1)) and DE405 + URA027 Titania ephemeris. The arrow indicates the direction of motion in the sky plane. The horizontal and vertical bars are aligned with the local celestial ICRS J2000.0 N–S and E–W directions, respectively, and have lengths of 1000 km, with celestial North up and celestial East left. The scale is 13,819 km per arcsec. Label "S" stands for Titania's south pole (IAU convention). Meridians and parallels on Titania's globe are plotted every 15°, with thicker lines delineating Titania's equator and origin of longitudes (the meridian facing Uranus). The intersection of this meridian with Titania's equator defines the sub-Uranus point on Titania, labeled "SU." Sub-observer latitude at Titania is −24.2°, and north pole position angle is 260.4°, see Table 1. An offset with respect to the expected Titania's position is clearly visible, see Section 4. The circle surrounding the chords is the best circular fit to Titania's limb (Section 5).

Titania's south pole was visible from Earth in the celestial East direction. As the uranian system was moving westward in the sky at the time of occultation, the star ingress occurred in the northern Titania hemisphere, close to equatorial and mid-northern latitudes (Fig. 7 *et seq.*). Egress occurred in the southern Titania hemisphere, at higher planetocentric latitudes than during ingress, in fact near the satellite's south polar region. Because the titaniacentric elevation of the observer is B = −24.2°, the occultation could probe latitudes between +65.8° and −65.8°.

Titania's offset is derived from a subset of ingress and egress times provided in Table 2. Each time gives the position of the observer in Titania's shadow at ingress or egress, once the star position at epoch is established (Eq. (1)). Titania's motion in right ascension and declination is interpolated using a sond-order polynomial, fitting twenty position steps calculated every minute and bracketing the event.

Practically, and owing to the wide variety of methods used here (CCD imaging, video, driftscan, visual, etc.), we have to establish selection criteria on the timings provided by the observing teams, in order to derive an accurate ephemeris offset through limb fitting.

We start with all the occultation chords provided in Table 2, using all possible timings at face value. The resulting fifty-seven chords are shown in Fig. 7. Some of them have clearly wrong durations, due to various kinds of errors (wrong time base, confusions due to the nearby, brighter Uranus, especially for visual observations, etc.). Several chords appear to have correct durations, though, but are shifted in time due to errors in absolute time setup (due e.g. to delays of internet clocks, personal reaction timelags from manual stopwatch, misprints when writing reports, etc.). It is impossible to retrieve the exact origin of all those time shifts, and

of course, to correct them afterwards. Such chords may be of interest, though, as their durations are correct to within a fraction of a sond, i.e. a few kilometers in length. As such they can be included in a circular fit to Titania's limb, as described in the next section.

Thus, we have shifted all the chords along the direction of motion, so that all the chords have a common mediatrix.[1] If Titania's limb is circular and all the relative timings are correct, then all the extremities of the chords should lie on a common circle, after this procedure has been applied. Because of timing errors, as alluded to just before, and also due to possible topographic features along the limb, radial residuals $\Delta r = r_{i,\mathrm{obs}} - r_{\mathrm{ref}}$ with respect to a common circle of radius r_{ref} are observed.

To proceed forward, we have selected chords which have a residual radial dispersion $\Delta r < \pm 10$ km. This corresponds to an error of 0.5 to 2 s in chord duration, depending on the observer's location projected on Titania's limb. The 10 km limit is of course arbitrary, but it appears that the most deviant chords are also those which are derived from either one, or a combination of the following observing circumstances: (i) smaller instruments (less that 15 cm in diameter), (ii) large time steps (no fraction of sonds available), (iii) documented problems, and/or (iv) visual observations, for which post-occultation corrections are impossible to make.[2]

This step eliminates 14 chords, leaving us with 43 chords, shown in Fig. 8. The circle fitted to the chord extremities has been obtained iteratively. First we fit a circle to the chord extremities, then we shift the chords so that all their mediatrixes coincide with the circle diameter perpendicular to stellar motion, repeating that operation till the circle center varies by less than one kilometer. Once this is achieved, we obtain Titania's offset with respect to its predicted position.

This offset, readily visible in Fig. 8, amounts to $\Delta f = -1493$ km (sign meaning toward celestial west) and $\Delta g = -862$ km (toward celestial south). The internal accuracy of this offset is less than ∼10 km, after the selection criterium on Δr for the 43 chords, described before. This corresponds to less than one milli-arc-second (1 mas = 13.8 km at Titania's distance) and thus negligible compared to the accuracy on the star position of $\Delta\alpha\cos(\delta) = 7.4$ mas and $\Delta\delta = 5.7$ mas, see Eq. (1). In other words, the error bars on the offset is dominated by error bars on the star position, and not by the accuracy of our fit. With a range of 2.8504×10^9 km, Titania's offset with respect to the DE405 + GUST86 prediction amounts to:

$$\begin{cases} \Delta\alpha_T \cos(\delta_T) = -108 \pm 7 \text{ mas}, \\ \Delta\delta_T = -62 \pm 6 \text{ mas}. \end{cases} \tag{3}$$

Part of this offset is due to a general offset of Uranus barycenter with respect to DE405, and part is due to an offset in Titania's motion around Uranus. To find out which of Uranus' or Titania's offsets prevail, let us consider some alternative ephemerides to DE405 and GUST86. While GUST86 was fitted to observations made from 1911 to 1986, a new theory ("LA07") has been fitted to more recent observations made from 1948 to 2003 (including Voyager observations) for better predicting the mutual events of 2007, see Lainey (2008).

Titania's position with respect to Uranus on September 8, 2001 at 02 h UT, as given by GUST86, is: $X = 11.0532$ arcsec and $Y = 11.4900$ arcsec, eastward and northward of Uranus ICRS J2000.0

---

[1] The mediatrix of two points in a plane is the line equidistant to those two points.

[2] Two stations, however, have large radial residuals, while good accuracy is expected since ingress and egress timings come from video tapes with 0.15 to 0.35 m telescopes. They are the Almerim station (Portugal), with $\Delta t = 1.55$ s corresponding to radial residual $\Delta r = -28.8$ km, for an expected error $\leqslant 0.1$ s, and Sabadell-2 0.15 m station (Spain), with $\Delta t = 2.04$ s and $\Delta r = -20.4$ km, for a claimed accuracy of 0.2 s. No explanation has been given for these large residuals.

Table 3
Circular fit to 27 selected chords, Sep. 8, 2001 event. The free parameters of the fit are Titania's radius, $R_{T,occ}$, and the location of shadow center, as given by the offset Δf, Δg (see text).

Site[a]	Rec.[b]	Δt[c] (s)	Ingress			Egress			C/A[f] (km)	Δr[g] (km)
			Latitude[d] (deg)	f[e] (km)	g[e] (km)	Latitude[d] (deg)	f[e] (km)	g[e] (km)		
Arikok, 0.2 m	ccd	+0.093	+65.7	−2275.3	−957.8	−45.4	−973.7	−271.1	+279.6	−1.37
Worth Hill, 0.25 m	vid.	+0.243	+65.6	−2261.0	−1044.5	−50.4	−911.6	−330.2	+197.3	−0.05
Ponta D., 0.3 m	vid.	−0.531	+65.3	−2251.7	−1068.2	−52.0	−894.8	−354.1	+170.2	−3.17
Caracas, 0.125 m	vid.	−2.520	+59.5	−2184.4	−1248.3	−61.1	−784.9	−510.7	−020.1	+2.74
Chatellerault, 0.1 m	vis.	−0.378	+50.4	−2078.3	−1393.4	−65.6	−725.7	−678.1	−196.8	+1.57
Marinha G., 0.4 m	vid.	−0.415	+36.7	−1898.8	−1540.1	−62.5	−705.7	−911.3	−411.4	+1.56
Linhaceira, 0.25 m	vid.	+0.235	+33.0	−1846.4	−1565.3	−60.3	−714.5	−968.7	−458.1	−1.48
Salinas-1, 0.25 m	ccd	−0.381	+32.0	−1833.6	−1573.5	−59.8	−714.6	−981.7	−470.4	+0.25
Salinas-2, 0.2 m	ccd	−0.333	+32.0	−1833.7	−1573.5	−59.8	−714.6	−981.6	−470.4	+0.29
Pic du Midi, 1 m	vid.	+0.290	+28.8	−1787.4	−1595.3	−57.5	−722.8	−1033.0	−511.6	+1.66
St. Maurice Caz., 0.2 m	vis.	−0.153	+23.2	−1705.3	−1619.9	−53.2	−748.5	−1114.1	−571.5	−1.21
Zaragoza, 0.12 m	vis.	−0.018	+22.6	−1696.0	−1624.5	−52.6	−750.3	−1125.3	−580.3	+0.78
Alvito, 0.25 m	vid.	+0.455	+22.4	−1693.2	−1626.1	−52.4	−751.0	−1129.7	−583.4	+1.59
Hortoneda, 0.203 m	vis.	+2.808	+19.7	−1652.6	−1631.8	−50.2	−768.6	−1165.0	−606.9	−2.02
COAA, 0.2 m	vid.	+0.402	+15.5	−1590.6	−1643.3	−46.5	−794.9	−1224.2	−646.5	−0.81
Portimão-1, 0.25 m	ccd	+0.007	+15.0	−1583.0	−1642.8	−46.0	−799.6	−1230.2	−649.6	−2.19
Orfeuilles, 0.2 m	vis.	−0.431	+11.5	−1529.6	−1647.1	−43.0	−824.9	−1274.6	−677.7	−2.04
St. Esteve, 0.2 m	vis.	+0.265	+07.8	−1473.4	−1648.6	−39.5	−855.8	−1322.5	−705.5	−1.09
Sabadell-1, 0.5 m	ccd	+0.097	+07.4	−1467.7	−1649.5	−39.1	−858.3	−1327.6	−708.9	−0.08
Barcelona-2.1, 0.21 m	vis.	+0.091	+06.5	−1453.4	−1648.5	−38.3	−867.2	−1338.9	−714.7	−0.49
Barcelona-2.2, 0.203 m	vis.	+0.041	+06.5	−1454.3	−1649.0	−38.3	−866.3	−1338.4	−714.7	−0.04
Barcelona-2.3, 0.21 m	vis.	+0.241	+06.5	−1454.3	−1649.0	−38.3	−866.3	−1338.4	−714.7	−0.05
Alella, 0.24 m	vid.	+2.492	+05.8	−1443.1	−1652.4	−37.6	−869.8	−1349.6	−722.9	+4.01
Barcelona-1, 0.258 m	vis.	+0.384	+04.9	−1430.2	−1647.5	−36.8	−881.0	−1357.5	−724.7	+0.12
Barcelona-3, 0.1 m	vis.	+0.111	+04.9	−1430.8	−1648.7	−36.9	−879.8	−1357.7	−725.4	+1.24
Alcublas, 0.2 m	vis.	+0.255	−01.0	−1341.9	−1634.4	−31.1	−942.1	−1423.4	−754.3	−0.77
Castellón, 0.2 m	vis.	−0.046	−02.7	−1316.8	−1630.1	−29.5	−959.7	−1441.7	−762.3	+0.31

Note. Best fitting circle radius $R_T = 788.4$ km, center: $f_c = -1494.1$ km, $g_c = -861.6$ km, r.m.s. radial dispersion: 1.58 km, no oblateness detected. See text, Section 5 for details.
[a] See Table 2. Chords have been sorted in order of decreasing closest approach (C/A) distances. This corresponds from top to bottom in Fig. 11.
[b] Type of recording mode: CCD, vid. = video or vis. = visual.
[c] Applied time shift, see text for details.
[d] Sub-occultation titaniacentric latitude.
[e] Position in sky plane, see Fig. 11.
[f] Closest approach to shadow center. Positive means observer North of shadow center, negative otherwise.
[g] Radial residual to circular fit (plotted in Fig. 12).

position, respectively. A new theory LA07 gives $X = 11.0456$ arcsec and $Y = 11.5130$ arcsec. This yields a difference LA07 − GUST86 = −8 mas and +23 mas in right ascension and declination, respectively, with typical accuracy of 20–25 mas. This indicates that the offset given above (Eq. (3)) is dominated by Uranus barycentric offset. Taking the LA07 theory as reference, our astrometric reconstruction discussed above yields the following Uranus offset, in the sense [our occultation observation minus DE405] of:

$$\begin{cases} \Delta\alpha_U \cos(\delta_U) = -100 \pm 25 \text{ mas}, \\ \Delta\delta_U = -85 \pm 25 \text{ mas}. \end{cases} \tag{4}$$

A survey made at the Bordeaux meridian transit circle actually shows that Uranus' offset averaged over several months around September 2001 amounts to: $\Delta\alpha_U \cos(\delta_U) = -98 \pm 10$ mas and $\Delta\delta_U = -122 \pm 10$ mas, see Arlot et al. (2008). This is fully consistent with our result in right ascension (difference of +2 mas with respect to our result), while the difference is barely significant in declination (difference of −37 mas).

We may finally compare the DE405 ephemeris with the newly released IMCCE ephemeris "INPOP06" (Fienga et al., 2008), which improves Uranus ephemeris. We have, in the sense [INPOP–DE405]: $\Delta\alpha_U \cos(\delta_U) = -66$ mas and $\Delta\delta_U = -75$ mas. There is now a barely significant difference (+34 mas) in right ascension when compared to our result, and a fully consistent offset in declination (difference +10 mas with our result).

4.2. Additional offset constraints from the Aug. 1, 2003 event

We have a confirmation of this systematic offset from another stellar occultation by Titania, observed on August 1st, 2003 (Fig. 9). The star involved, TYC 5806-696-1 (V = 10.3) has the following ICRF position at epoch, $\alpha = 333.9773096° \pm 20$ mas and $\delta = -11.6156551° \pm 13$ mas (Table 1) with proper motion taken into account as for HIP 106829 on September 8, 2001, but not annual parallax, which is too small to be measured. The 2003 event was observed from two sites, in Mexico and USA, see Table 4 for locations, instrument characteristics and timings. With these two chords, we obtain a radius for Titania of 787.3 km, i.e. 1.1 km smaller than the radius obtained later in this paper, but with an uncertainty of ∼4 km, vs a fraction of km obtained with the September 2001 event. So, this occultation does not improve our radius determination presented in the next section. However, the timing of the event is reliable enough to provide a significant Titania offset of -127 ± 20 mas and -97 ± 13 mas, where error bars come again from uncertainties on the star position. This offset is fully consistent in right ascension with the offset obtained in 2001 (see Eq. (3)), and barely larger—in absolute value—in declination. This difference remains marginal, however, when compared to error bars.

In summary, the offset established for the Sep. 8, 2001 occultation and confirmed by the Aug. 1, 2003 occultation is probably a manifestation of Uranus' offset slowly varying over years with respect to the DE405 ephemeris for the main part, and from Titania's uranocentric orbit for a small part.

Table 4

Titania occultation, August 1, 2003, circumstances and timings. Same abbreviations as in Table 2.

Site name	Lat. (d:m:s), lon. (d:m:s), alt. (m)	Ingress UT, egress UT, cycle time	Telescope, instrument/receptor, timing ref. and remarks	Observers
		Mexico		
Observatorio UANL	25:54:51.5 N 100:08:35.6 W 385 m	04:28:08.49 ± 0.05 04:29:22.01 ± 0.03 ±0.05/0.03 s	R 0.3 m S/C, Astrovid video with GPS time insertion	P. Valdés Sada, R. Hernández, E. Castro
		United States of America		
George Observatory	29:22:30 N 95:35:37 W 24 m	04:27:53 ± 1 04:28:53 ± 1 ±1 s	R 0.9 m S/C, video with WWVB time signal	A. Hernández, P. Maley, B. Wilson
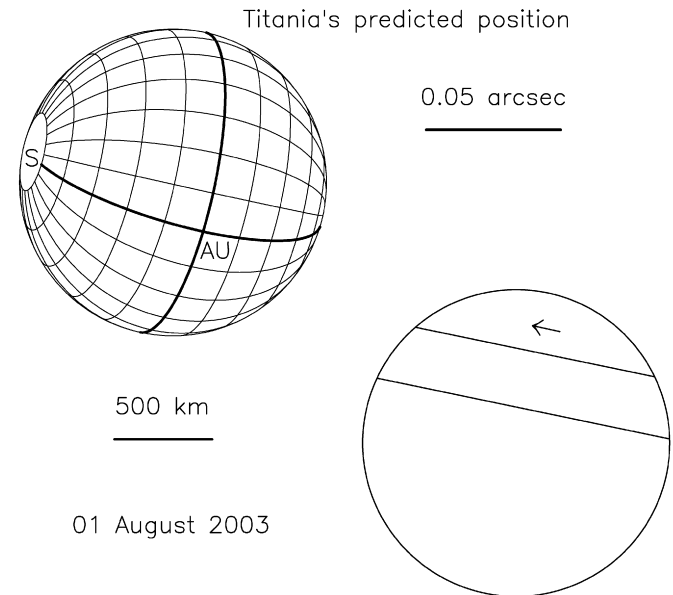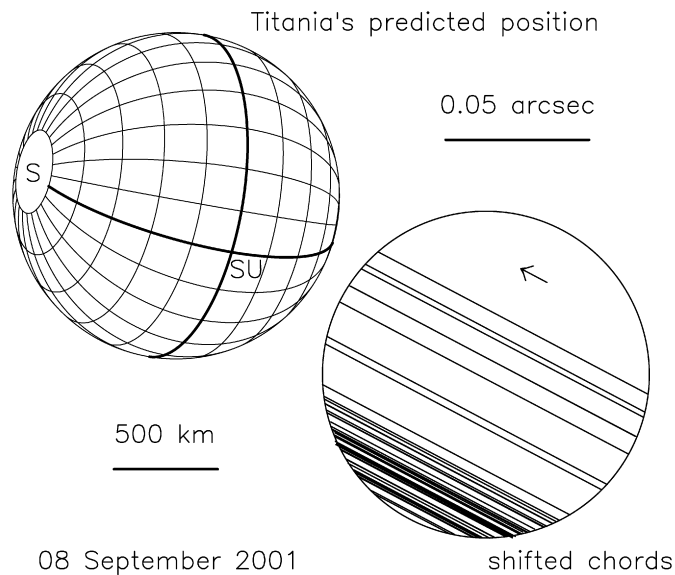
Fig. 8. Same as Fig. 7, but limited to the forty-three stations with radial residual $\Delta r = r - r_{\text{ref}} \leqslant 10$ km used for Titania's ephemeris offset determination (Table 2 and Section 4). This corresponds to an error of 0.5 to 2 s in chord duration, depending on the observer's location projected on the limb. The occultation chords have also been displaced along their own direction so that they share the same mediatrix. This is equivalent to applying a time shift to each of those stations, to compensate for their absolute timing error, see text for details. The offset in ICRS J2000.0 celestial coordinates, between Titania's expected position (globe at upper left) and observed position is $\Delta\alpha \cos(\delta) = -108 \pm 13$ mas and $\Delta\delta = -62 \pm 7$ mas. Like in Fig. 7 the circle surrounding the chords is the best circular fit to Titania's limb.

Fig. 9. The two occultation chords derived from the additional timings provided by the Aug. 1, 2003 occultation (see Table 4) and used for an additional offset constraint to Titania's ephemeris position. The figure shows Titania's orientation and direction of motion in the sky plane in ICRS J2000.0 coordinates. Label "S" is Titania's south pole; titaniacentric meridians and parallels are plotted every 15°. "AU" designates the anti-suburanian meridian at longitude 180°, as prime meridian is on the far side. See text, Section 4 for details.

5. Titania's size and upper limit on oblateness

The next step of our analysis involves further selection among observed chords, in order to increase the accuracy on Titania's size and shape. We keep the observations for which (i) frame by frame data acquisition and timing capability is provided, using a CCD or a video/camcorder equipment and (ii) visual observations and timings reported with radial residuals consistent with $\Delta r < \pm 5$ km, allowing us to obtain an improved timing of the star ingress and egress. Consequently, we eliminate timings obtained from drift scans observations, as the time interval during which the stellar trail disappears is actually affected by the point spread function (PSF). For instance, the occultation durations derived from the two IOC cameras at Salinas 1–2 (Ecuador) agree with each other to within 0.005 s, while the drift scan observation made at the same site (Salinas-3, Ecuador) shows a large discrepancy of 1.8 s, see Table 2, corresponding in that case to a difference in chord length of about 30 km. Although it might be possible to correct the effect of PSF convolution in the occultation length, even in that case, estimation of error bars would be problematic.

We noticed that the radial dispersion of the chord extremities show a marked concentration in an interval $\Delta r = \pm 5$ km (Fig. 10), with some outliers between 5 and 10 km, that we have withdrawn from the fit. We therefore retained $\Delta r < \pm 5$ km as a selection criterium for the limb fitting analysis. All outliers, from the previous selection of 43 stations, except two, are from visual observations, for which it is now impossible to assess the degree of confidence. For the two remaining stations excluded with that method, Observatoire de Haute Provence (France) and Oeiras (Portugal), no satisfactory explanations have been given for their larger radial residuals.[3] In contrast, we kept 13 visual observations reported by experienced observers for which we estimate an accuracy of about 0.2–0.3 s for the occultation duration (even if the absolute timing may be off by much more than that, as detailed in Table 3). To support why the remaining visual timings may equal the relative accuracy of frame-by-frame recording, on can note in Fig. 11 that many remaining visual chords (shown in black solid) are far away from shadow center, which may reduce significantly the projected star velocity perpendicular to the limb down to 6–14 km s^{-1}, depending on the chord. Consequently, typical errors

---

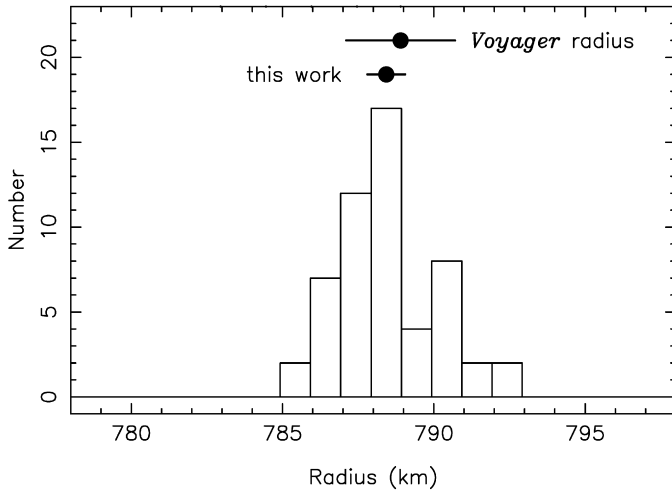[3] $\Delta r = +5.0$ and -8.8 km, respectively.

Fig. 10. Histogram of radial residuals for our best circular fit to both extremities of the twenty-seven occultations chords of Fig. 11, reported in Table 3. Our fitted Titania's radius, $R_{T,\text{occ}} = 788.4 \pm 0.6$ km, is shown as a black dot with associated error bars, just below the value derived from *Voyager* images, $R_{T,\text{Voy}} = 788.9 \pm 1.8$ (Thomas, 1988). Most of the dispersion seen in this histogram is likely to be caused by topographic features along Titania's limb, see Section 5, Subsection 5.1.

of 0.2–0.3 translate into radial residuals of typically 1–4 km, i.e. less than the 5 km limit we used to discriminate the CCD or video frame-by-frame observations for limb fitting, as explained above.

5.1. Circular fit

Twenty-seven occultation chords are finally kept for a circular limb fit. They consist in a total of 13 visual timing observations, 9 video recordings and 5 CCD recordings, plotted in Fig. 11 and listed in Table 3. A first point to note is that even with the stations with the best timing accuracies, the radial residuals to a circular fit are quite larger than the expected accuracy of each measurements. For instance, the Salinas-1, Salinas-2, Arikok, Pic du Midi and Portimão-1 chord extremities have formal radial accuracies of 0.1 to 0.4 km, while the observed radial residuals have values of $\Delta r = \pm 2$ km.

This indicates either that we grossly underestimate our error bars, or that this dispersion has a physical origin, not accounted for by our circular fit. This will be discussed later, but we can already mention here that images taken by the *Voyager* spacecraft in 1986 show typical r.m.s. limb radial dispersions of ± 1 km, with peak to peak amplitudes of ± 3 km (Thomas, 1988). Our r.m.s. residuals of $\Delta r = \pm 2$ km are thus consistent with the *Voyager* images and are typical of what may be expected from the satellite topography itself, characterized by scarps 2–4 km high and an uneven crust. In other words, the pseudo random radial fluctuations that we observe are likely to be dominated by Titania's topography, not by the uncertainties on the durations of our 27 selected chords. There are only two stations for which the error bars exceed the typical limb radial dispersion, namely the Ponta Delgada (Azores Island, Portugal) and Marinha Grande (mainland Portugal) sites. Their timing accuracy is announced at ± 0.3 and ± 0.5 s, respectively, translating into radial accuracy of 3.1 and 4.1 km, respectively.

We now proceed to a circular fit to the extremities of the 27 selected chords. The free parameters of the fit are Titania's radius, $R_{T,\text{occ}}$, and the location of shadow center, as given by the offset $(\Delta f, \Delta g)$. We define the χ^2 of the fit as:

$$\chi^2 = \sum_{i=1}^{54} \frac{(r_{i,\text{obs}} - R_{T,\text{occ}})^2}{\sigma_i^2}, \tag{5}$$

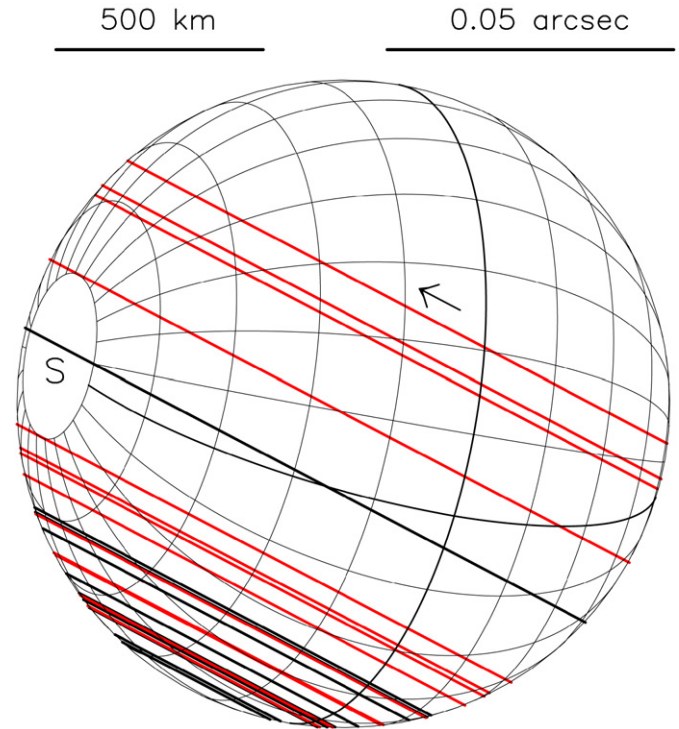where the $r_{i,\text{obs}}$'s are the 54 radii of the 27 chords extremities.

Fig. 11. The twenty-seven occultation chords used for Titania's size and oblateness determination through limb fitting (see Section 5). The free parameters of the fit are Titania's radius, $R_{T,\text{occ}}$, and the location of shadow center, as given by the offset $(\Delta f, \Delta g)$. Time shifted chords have been superimposed on a figure of Titania that has been shifted by the ephemeris corrections in Eq. (3). Corresponding ground stations are listed as a subset of Table 2 (footnote "d"). Among them are thirteen visual observations (thin lines, black in the online version). Bold lines (red in the online version) indicate chords obtained from electronic, frame-by-frame recording of the event (CCD or video), Table 3 lists the applied time shift, sub-occultation titaniacentric latitude coordinate of ingress and egress points, closest approach to shadow center and radial residuals Δr.

We will assume that the error σ_i^2 attached to each chord length is imposed by Titania's topography. Our best circular fit to the 27 selected chords then yields a radius $R_{T,\text{occ}} = 788.4$ km, with a dispersion of 1.6 km (Fig. 11). Since we shifted the chords prior to the fit so that they have a common mediatrix, the two extremities of a given chord have the same radius, by definition. Consequently, there are actually $N = 27$ independent data points, while the fit has $M = 3$ adjusted parameters ($R_{T,\text{occ}}$, Δf and Δg), so that the expected minimum value of χ^2 is the number of degrees of freedom, $\chi^2_{\min} = \nu = N - M = 24$.

This value is obtained for $\sigma_i = 2.29$ km, a value that we keep for our error bar determination, except for the Ponta Delgada and Marinha Grande chords, for which we take 3.1 and 4.1 km, as explained before. Exploring the effect of fixed values of $R_{T,\text{occ}}$ on χ^2, while keeping Δf and Δg as free parameters, we obtain the so-called 1-σ error bar (68.3% confidence level) for $R_{T,\text{occ}}$, such that $\Delta \chi^2 = \chi^2 - \chi^2_{\min} = 1$ (Press et al., 1986):

$$R_{T,\text{occ}} = 788.4 \pm 0.6 \text{ km}. \tag{6}$$

This radius is fully compatible with the value derived by Thomas (1988) from the *Voyager* images $R_{T,\text{Voy}} = 788.9 \pm 1.8$ km. This latter value is actually an average of seven limb profiles, none of them being *a priori* the one that we observed during the occultation.

We finally derive a mean density $\rho = 1.711 \pm 0.005$ g cm^{-3} for Titania, based on Taylor (1998) estimate of $GM = 2.343 \times 10^{11}$ m^3 s^{-2} (Table 1). It lies within previously published value using *Voyager*'s radius $R_{T,\text{Voy}} = 788.9 \pm 1.8$ (Thomas, 1988) and improves by a factor of 10 the value of $\rho = 1.71 \pm 0.05$ g cm^{-3}
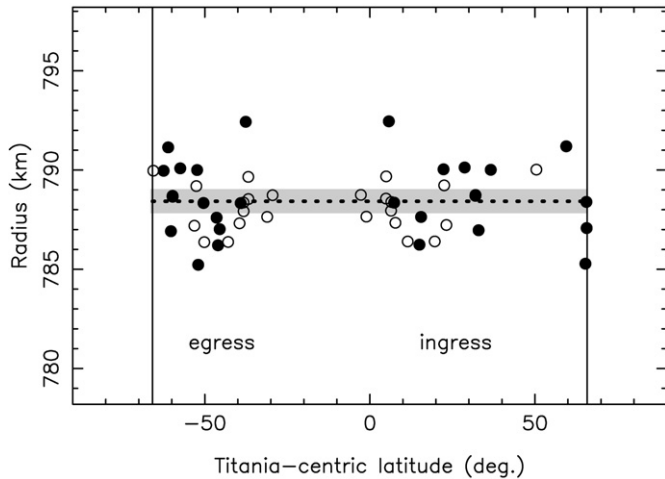
Fig. 12. Upper limit on Titania's oblateness. X-axis is the titaniacentric latitude, with South pole on the left and North pole on the right, from −90° to +90°. Y-axis is the distance of chords extremities (see Fig. 11) to Titania's shadow center. The dotted horizontal line corresponds to the radius of our best circular fit, $R_{T,occ} = 788.4 \pm 0.6$ km, with its error bar (± 0.6 km, shaded rectangle). Bullets indicate the ingress and egress distances $r_{i,\mathrm{obs}}$ versus sub-occultation latitude on Titania, after each 27 chords has been shifted in absolute time so they have a common mediatrix. This explains why the points come by pairs (ingress at right and egress at left) with the same distance to shadow center imposing their extremities to have the same radial residuals with respect to a reference circle. The vertical lines marks the maximum latitudes ($\pm 65.8°$) reachable during the occultation, due to the titaniacentric elevation $B = -24.2°$ of the observers during the Sept. 8, 2001 event. Solid bullets are from the 14 stations with an electronic record of the event (CCD or video), while open bullets are from the 13 best visual observations, see Section 5.

by Jacobson et al. (1992). This density represents a silicate to ice ratio of ~0.5 (Brown et al., 1991), a much higher silicate fraction than the satellites of Saturn, in agreement with the observed relative depletion of surface ice in the uranian system, that we discuss in Section 6.

5.2. Upper limit on oblateness

Estimating the satellite oblateness is hampered by the fact we have shifted the occulting chords in time, so that they have a common mediatrix. In doing so, we impose the radial residuals to be the same at each extremity of a given chord, i.e. at two different latitudes. This tends to mix up any low frequency pattern present along the limb. This effect is visible in Fig. 12, where the points come by pairs with same radii.

However, we may give a rough estimation for the upper limit on oblateness in a simplified situation, namely assuming that Titania is an ellipsoid of revolution, with smaller axis aligned with its pole. At lowest order in oblateness $f = (r_{eq} - r_{po})/r_{eq}$, where r_{eq} (resp. r_{po}) is the equatorial (resp. polar) radius, the limb shape is given by $r = r_{eq}[1 - f \sin^2 \phi]$, where r is the radius at latitude ϕ. This limb profile is an even function of ϕ, so that the points of Fig. 12 can be all folded in the interval $[0°, 90°]$. Furthermore, each pair of point corresponding to one chord can be replaced by a unique point with same radial residual, at a latitude which is the average of the latitudes of the two points.

Fig. 13 shows the result of this operation. When the function $r_{eq}[1 - f \sin^2 \phi]$ is fitted to these data points, the overall radial residual is decreased. However, since one new free parameter is added (namely, the oblateness f), the χ^2 per degree of freedom of the fit actually increases, showing that no significant oblateness is detected in our data set. More precisely, we obtain an equator to pole difference of $r_{eq} - r_{po} = -1.3 \pm 2.1$ km, while the equatorial radius remains close to the circular fit value, $r_{eq} = 788.0 \pm 0.9$ km.
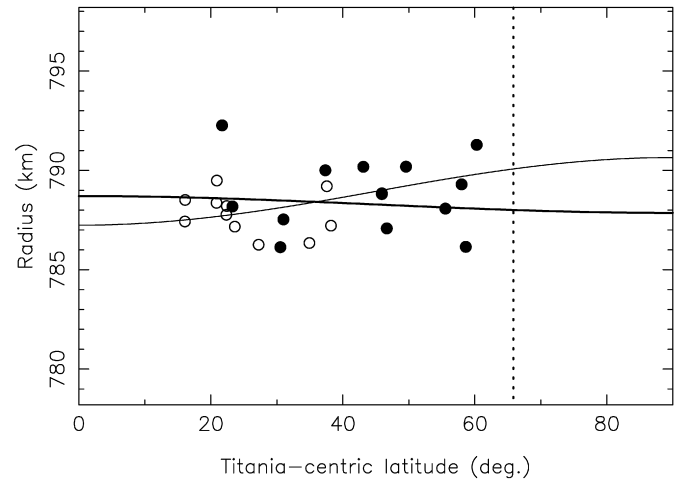

Fig. 13. Same as Fig. 12, after plotting all latitudes in absolute value, and averaging them over ingress and egress values. The thicker line corresponds to the upper limit of an oblate limb of the form $r = r_{eq}[1 - f \sin^2 \phi]$, with a difference between equatorial and polar radius of $r_{eq} - r_{po} = +0.8$ km. The thin line is the upper limit of a prolate limb, with $r_{eq} - r_{po} = -3.4$ km. See text for details.

A rough estimation of the oblateness f of a slowly rotating fluid satellite is given by $f \sim q$ (Murray and Dermott, 1999), where q is the dimensionless rotational factor $q = (4\pi^2 R^3)/(GMP^2) \sim 1.5 \times 10^{-4}$, using the GM and rotation period $P = 8.706$ days (Table 1). This would imply a difference $r_{eq} - r_{po} \sim 0.1$ km, i.e., about 10 times smaller than the upper limit for $r_{eq} - r_{po}$ derived above from our data set. This finding is in agreement with *Voyager* limb image analysis by Thomas (1988) who find no observational evidence for oblateness. Another attempt was made in our analysis, assuming that Titania is elongated along the line joining the satellite to the planet (i.e. along the suburanian point labeled "SU" in Fig. 7). In this case, however, all the sub-occultation points along the limb lie between 63° and 90° away from the point SU. This is a too narrow interval to yield any significant constraint on a possible elongation towards Uranus. Other directions of elongation might be possible, but the shifts of the chords described earlier make impossible a detection of such distortions.

Note that without absolute timing shifts discussed before, we would have reached a much more stringent upper limit for Titania's oblateness. This is a strong argument for the importance of getting *absolute* timing accuracy at the 0.1 s level or less.

6. Limits on an atmosphere around Titania

In this section, we use the occultation data to constrain the existence of an atmosphere around Titania. Potential origins for such an atmosphere include (i) solar-induced ice sublimation, which is strongly dependent on the surface temperature, (ii) outgassing associated with hot-spot cryovolcanism. As discussed hereafter, the high sensitivity of occultation lightcurves to vertical refractivity variations allows us to derive significant constraints (upper limits) on an atmosphere.

6.1. Derivation of an initial atmospheric limit based on radius

A remarkable feature of this particular event, is the fact that we can directly compare a ground-based observation with remote sensing observations from a nearby spacecraft. The excellent agreement between the two results is a strong illustration of the power of ground-based observations, for which kilometric accuracies or better can be reached.

We used the *Voyager* radius of $R_{T,\mathrm{Voy}} = 788.9 \pm 1.8$ km as a reference as its value derived by Thomas (1988) results from images
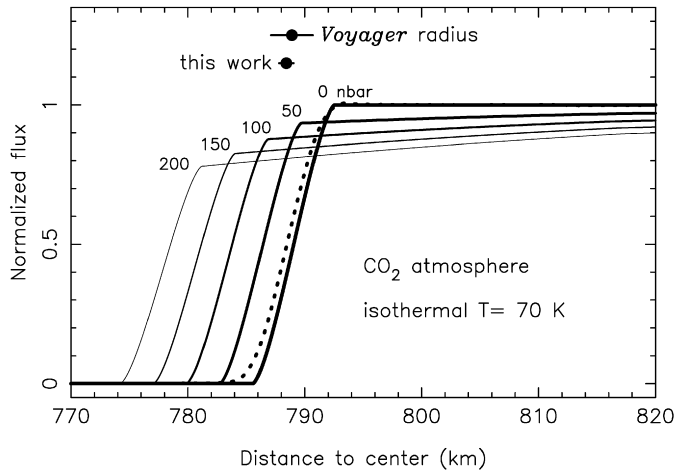
Fig. 14. Examples of shrinking of Titania's shadow radius due to ray bending by a model CO_2 isothermal atmosphere ($T = 70$ K) with surface pressures of 0, 50, 100, 150, 200 nbar, in order of decreasing line thicknesses, see also labels above each curve. The model takes into account the smoothing by a 0.51 mas diameter star (but does not account for diffraction effects), and assumes the radius derived from *Voyager* images, 788.9 km (Thomas, 1988). The *Voyager* radius and our own measurement are shown by black dots with associated error bars at the top. The dotted line is the diffracting model which best fits our data, see Fig. 5. For this particular model (CO_2 at $T = 70$ K), we find that Titania's apparent radius decreases by about 0.056 km *per* nbar added to the surface pressure. The stellar drop just prior to the occultation by Titania's limb amounts to about 1.1×10^{-3} *per* nbar. For instance, a 200 nbar atmosphere shrinks the radius by about 11.2 km, and causes a drop of 22% by the time the star reaches the satellite limb. See text, Section 6, Subsection 6.1.

acquired during the 1986 flyby with no detectable atmospheric effect on the limb at close range. The difference of radii derived from our experiment and from *Voyager*, $\Delta R = R_{T,\text{occ}} - R_{T,\text{Voy}} = -0.5 \pm 1.9$ km, is not significant, but can nevertheless be used to set an upper limit of a faint atmosphere around Titania.[4] Such a tenuous atmosphere could actually refract the stellar rays, reducing the shadow radius at Earth, with respect to the actual radius. This effect is illustrated in Fig. 14, where various occultation profiles are generated, assuming isothermal ($T = 70$ K) CO_2 atmospheres with surface pressures of 0, 50, 100, 150 and 200 nbar. Those profiles are obtained by ray tracing, using a procedure described in details by Sicardy et al. (2006). The upper limit for the difference between *Voyager*'s and our measurement, $\Delta R \leqslant 2.4$ km sets a 1-σ upper limit of $p_s = 45$ nbar for the surface pressure of such a CO_2 atmosphere. One must be careful, however, that we did not observe the same limb as *Voyager* did, and that difference of 3–4 km are still possible, depending on the geometry of observation (Thomas, 1988). So, a value of $p_s = 70$ nbar seems a safer 1-σ upper limit for a CO_2 atmosphere at $T = 70$ K, based on the upper limit of apparent shrinking of Titania's mean radius, see Fig. 14. A tighter upper limit for an atmosphere around Uranus' largest moon can be inferred from the stellar flux refracted prior to, and after the stellar occultation by Titania's limb, as we examine in the next subsection.

6.2. Upper limits on the surface pressure based on lightcurves

Interpreting stellar occultation lightcurves in terms of atmospheric properties requires an assumption on its composition. A sublimation atmosphere reflects the composition of the surface. Near infrared spectroscopy has demonstrated the presence of water ice (e.g. Grundy et al., 1999, for the most recent study) and

---

[4] Ray bending by Titania's gravitational mass, due to general relativity, amounts to only 50 m or so at the Earth's distance, and is thus irrelevant at our level of accuracy.

Table 5
Modeling results for Titania's atmosphere surface pressure at equilibrium, with detection upper limits in standard deviation units for CO_2, CH_4 and N_2.

Gas	$(dz/dT)_z$ (K km^{-1})	$T (z > 20$ km) (K)	Surface scale height (km)		Surface pressure upper limit (nb)	Column density (cm-amagat)
CO_2	0	60	30	1-σ	9	0.132
				3-σ	20	0.293
CO_2	0	70	35	1-σ	13	0.193
				3-σ	28	0.410
CO_2	0	80	40	1-σ	17	0.257
				3-σ	37	0.549
CH_4	2	110	95	1-σ	8	0.436
				3-σ	18	0.954
N_2	0	70	55	1-σ	22	0.550
				3-σ	46	1.150

carbon dioxide (Grundy et al., 2006) on the surface of Titania (and Ariel, Umbriel and Oberon, with no detected CO_2 on Oberon). While H_2O ice is clearly involatile, CO_2 ice stability against sublimation over the course of a seasonal cycle of Titania can be considered. As shown by Grundy et al. (2006), its vapor pressure of about $p_{CO_2} = 1.6 \times 10^{-4}$ nbar for a mean surface temperature of $T = 70$ K is sufficient to induce significant sublimation-condensation cycles and seasonal redistribution.

We thus consider a CO_2 atmosphere as our baseline case. Deriving a constraint on the surface pressure requires the knowledge of carbon dioxide molecular refractivity (Table 1) and an assumption on the vertical temperature profile. We assumed isothermal atmospheres at temperatures of 60, 70, and 80 K. These are in the range of (i) the H_2O ice temperatures measured from the near-IR spectra (Grundy et al., 1999) and (ii) the mean 20-μm brightness temperature (70 ± 7 K) determined by Brown et al. (1982). Due to the very small pressures involved, the atmosphere must be transparent to surface thermal radiation, so we did not consider tropospheric or mesospheric cooling. With a surface gravity of 0.38 m s^{-2}, the assumed surface temperatures correspond to pressure scale heights of 30, 34, and 39 km respectively.

To perform model fitting we have combined the stellar fluxes observed in four of our IOC datasets in Arikok (Aruba), Salinas-1 and -2 (Ecuador) and Portimão-1 (Portugal). All data points with $r > 792$ km were included in the fit, to the limit of significant signal drop due to partial occultation of the stellar disk by the limb, so the star remains essentially unocculted. Ingress and egress measurements were folded over, and data sets from different stations were separately fitted, taking into account their individual noise levels. The synthetic lightcurves were obtained by ray tracing, see Sicardy et al. (2006) for details. We calculate the χ^2 while keeping CO_2 ground pressure as free parameter, and determine the upper limit at 1-σ error bar (68.3% confidence level) so that $\Delta \chi^2 = \chi^2 - \chi^2_{\text{min}} = 1$. For a pure CO_2 isothermal atmosphere with $T = 60$ K, we find a maximum surface pressure $p = 9$ nbar. The corresponding atmospheric column density is 0.132 cm-amagat. The 1-σ pressure upper limit is 13 nbar for $T = 70$ K, and $p = 17$ nbar for $T = 80$ K (Table 5). Fig. 15 illustrates the effect on the light curve of an isothermal, $T = 80$ K pure CO_2 atmosphere. In this figure, the shaded area shows the difference between this upper-limit of 1-σ and an airless model. As the contribution to errors of each data point depends not only of its uncertainty, but also on the relative velocity of the star, perpendicularly to the limb, we have binned the folded-over data from the four stations at constant radius intervals $\Delta r \sim 20$ km. Note that the binning has been performed for plotting purposes only in order to readily reflect the contribution of each lightcurve to the atmospheric detection (Fig. 15).

We explored the possibility of other, more volatile, constituents, namely CH_4 and N_2. Although such compounds are unlikely to be
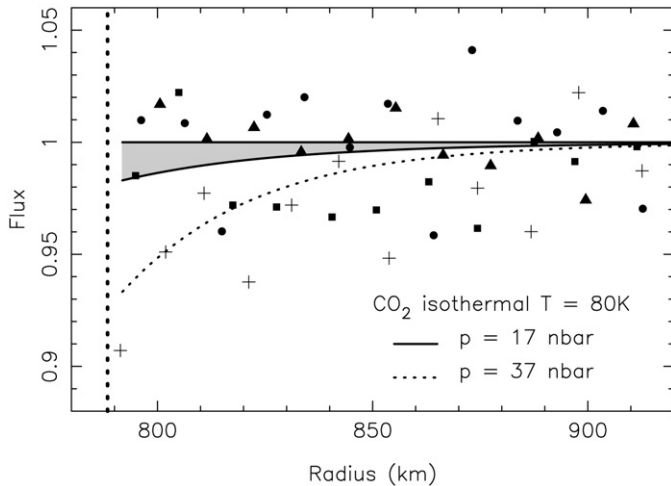
Fig. 15. Same as Fig. 5, but at different scales, to illustrate the effect of a faint atmosphere on the light curves. Symbols are the same as in Fig. 5, namely Salinas-1 0.25 m (squares), Salinas-2 0.20 m (bullets), Arikok 0.20 m (triangles) and Portimão-1 0.25 m (crosses). For each of the four lightcurves, the before-ingress and after-egress data points have been folded over and binned over ∼20 km vertical bins, in order to take into account the relative velocity of the star perpendicularly to each limb, so that the radial sampling Δr is constant at each station on the plot. In this way the actual contribution of stations to vertical sampling can be assessed, although the fit to model was performed on *actual* data points. The point on left (Portimão) corresponds to the stellar drop behind Titania's limb at $r < 792$ km (those data points were *not* included in the fit). The dotted vertical line corresponds to our estimate of Titania's radius best value of 788.4 km. The smooth solid line is the 1-σ upper limit for the fit of actual data points to a CO_2 isothermal ($T = 80$ K) model atmosphere, with a surface pressure of 17 nbar. The dotted line is the 3-σ upper limit ($p = 27$ nbar). The shaded area shows the difference between this model and an airless model. See Table 5 and text for details.

present as a permanent, stratified atmosphere given the unstability of their surface frosts (see below), they could be temporarily present as possible products of outgassing associated with internal heating and cryovolcanism. For a pure CH_4 atmosphere, we assumed a "Pluto-like" stratosphere, produced by absorption of solar near-IR radiation. For definiteness, we adopted a temperature profile increasing from $T = 70$ K at the surface to an isothermal $T = 110$ K above 20 km. The resulting scale height is $H = 95$ km at the surface. In this case, the 1-σ detection upper limit is $p = 8$ nbar (Fig. 16), corresponding to an atmospheric column density of 0.44 cm-amagat. For a pure N_2 atmosphere, assumed isothermal at 70 K (scale height $H = 55$ km), we find an upper limit $p = 22$ nbar with a corresponding atmospheric column density of 0.55 cm-amagat (Fig. 17). In Figs. 15–17, we have included as a smooth dotted line, the expected lightcurve for a detection event at 3-σ ($p = 18$ nbar for CH_4, $p = 27$ nbar for CO_2 with $T = 80$ K, $p = 46$ nbar for N_2). Results are summarized in Table 5.

6.3. Discussion

As detailed above, we determine 1-σ upper limits of an atmosphere around Titania at the level of 10–20 nbar. Is it physically significant? For a sublimation equilibrium atmosphere, the equilibrium pressure is a very steep function of the temperature. Based on saturation laws described by Brown and Ziegler (1980), CO_2 vapor pressure p_{CO_2} is orders of magnitude below our derived surface pressure upper limits at $T = 70$ K. However, the surface temperature may be locally higher than this mean value. For example, Hanel et al. (1986) have measured maximum, sub-solar, temperatures of 86 ± 1 and 84 ± 1 K at Miranda and Ariel from Voyager 2/IRIS measurements. Although no values are reported for Titania in that paper, even slightly higher values may be expected because Titania's Bond albedo may be slightly lower (0.15 ± 0.02) than Miranda's (0.18 ± 0.05) and Ariel's (0.20 ± 0.04), see Helfenstein et
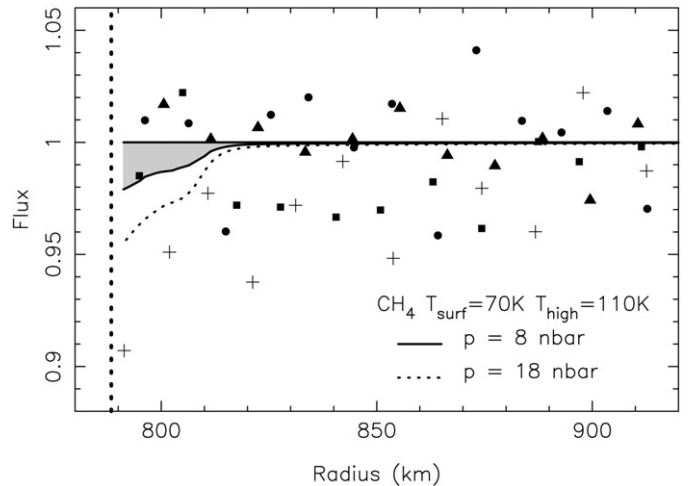

Fig. 16. Same as Fig. 15, but for methane. The smooth solid line is the 1-σ upper limit for a heated CH_4 atmosphere with $T = 70$ K at surface level and $T = 110$ K above 20 km, with a surface pressure of 8 nbar. The shaded area shows the difference between this model and an airless model, while the dotted line shows the 3-σ upper limit ($p = 18$ nbar) for comparison. See Table 5 and text for details.

al. (1988) and Buratti et al. (1990). In fact, the maximum surface temperature that can be expected on Titania is given by the instantaneous equilibrium with solar input, as:

$$T = \left(\frac{\Phi_0 (1 - A_B)}{\epsilon_B \sigma r_h^2} \right)^{1/4}, \tag{7}$$

where Φ_0 is the solar constant, A_B is Bond's bolometric albedo, r_h is the distance to the Sun, σ is Stefan–Boltzmann's constant and ϵ_B is the bolometric emissivity. With $\epsilon_B = 0.9$, the maximum possible temperature on Titania is 88.6 K. At this extreme temperature, $p_{CO_2} = 2.9$ nbar (Brown and Ziegler, 1980), still a factor of 3–6 lower than the upper limit provided by our measurement. Thus, it is not surprising that we are unable to detect an equilibrium CO_2 atmosphere around Titania. We note also that the *Voyager* measurements were acquired at southern summer solstice, which is the period of maximum surface temperatures (in polar regions).

The situation is very different for N_2 and CH_4, for which an equilibrium pressure of ∼10 nbar is reached for temperatures as low as 29 and 38 K, respectively. However, the problem is rather that Titania is too small to retain N_2 or CH_4 ices against a massive thermal evaporation, given their high volatility (Jeans escape is proportional to equilibrium vapor pressure). Schaller and Brown (2007a) have recently examined the volatile loss and retention on distant icy (Kuiper Belt) Solar System objects. They find that a ∼800 km object is able to retain its volatiles (N_2, CH_4, CO) over the age of the Solar System only if its "equivalent" temperature (essentially their perihelion temperature) is less than ∼30 K. Clearly, an equilibrium atmosphere of N_2 and CH_4 is not expected on Titania, consistent with the absence of features due to their ices in its near-infrared spectrum.

Although the above arguments seem to rule out a significant sublimation atmosphere on Titania, there remains, in principle, the possibility of a plume-like atmosphere, similar to Enceladus'— where the above discussion would apply as well. In Enceladus' southern pole plume, Cassini /INMS measurements have indeed revealed the presence of volatile and involatile species, namely 91% H_2O, 4% N_2, 3% CO_2 and 1.6% CH_4, with a total pressure in the range 10^{-1}–10^{-4} nbar (Waite et al., 2006). Another estimate of gas density within the plume was obtained from the stellar occultation of γ Orionis on July 14, 2005, observed with Cassini UVIS (Hansen et al., 2006), showing evidence for water vapor absorption, with a slant abundance of 1.5×10^{16} cm^{-2}, and an exponen-
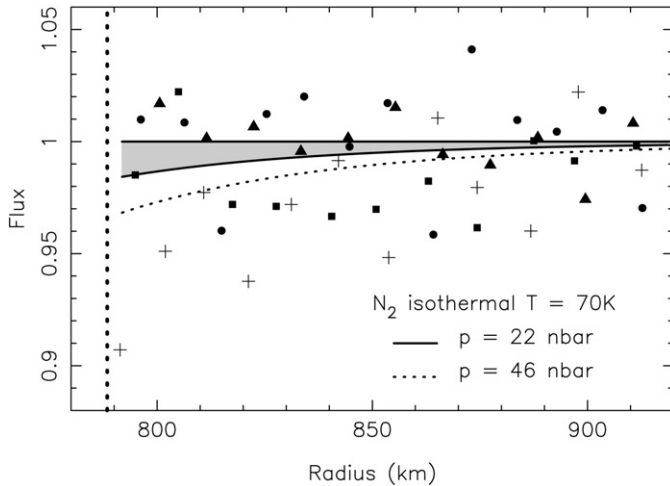
Fig. 17. Same as Fig. 16, but for an isothermal, $T = 70$ K N_2 atmosphere. The 1-σ upper limit is 22 nbar, corresponding to 0.550 cm-amagat (solid line) while the 3-σ upper limit corresponds to $p = 46$ nbar or 1.150 cm-amagat (dotted line).

tial decline of slant column abundance versus altitude with a scale length of 80 km. From this, a $\sim9 \times 10^{15}$ cm^{-2} vertical column and a $\sim10^9$ cm^{-3} surface density can be roughly estimated.

Converting this into a surface pressure would require an assumption on the unknown gas temperature, but for a gas temperature in the range 100–1000 K, the above numbers typically indicate a 0.01–0.1 nbar atmosphere. This remains significantly less than our upper limits. Titania's surface is poorly constrained by its geological features: comparison with other major uranian satellites suggests it was globally resurfaced up to 2 Ga ago (Croft and Soderblom, 1991, see also Fig. 10 in Zahnle et al., 2003). Crystalline water deposits may be considered as a possible indicator of recent heating episodes (e.g. Jewitt and Luu, 2004), and relatively high destruction and loss rates of CO_2 ice suggest a possible recent or ongoing source (Grundy et al., 2006). However, the presence of CO_2 ice does not seem to correlate with less-cratered, younger regions and no convincing evidence can be found for outgassing activity. This is opposed to Enceladus, where an age of 10–100 million years is estimated for the southern polar region (Porco et al., 2006), and probably even much younger for the "Tiger stripes" features from which the plume seems to originate.

In summary, the non-detection of an atmosphere of Titania is not surprising. However, our search demonstrates the power of the occultation technique to probe atmospheres down to pressure levels of ~10 nbar, much more tenuous than on Pluto or Triton, by typical factors of 10^3. This is promising in view of the detection of volatile ices on several trans-neptunian objects (TNO's). Methane has been clearly detected on dwarf planets Eris (e.g. Licandro et al., 2006b), Makemake formerly known as 2005 FY_9 (Licandro et al., 2006a), and recently on Quaoar (Schaller and Brown, 2007b), while the presence of N_2 on Eris is indirectly suggested (Licandro et al., 2006b; Dumas et al., 2007). At a current distance of 43 AU, and with its large size (1260 ± 190 km) which makes its ices marginally stable over the age of the Solar System (Schaller and Brown, 2007a), Quaoar appears to be a promising occultation target for an atmosphere.

On a longer term, a monitoring of TNO atmospheres might reveal a seasonal variability due to sublimation–condensation exchanges, as has been observed on Pluto (Elliot et al., 2003, 2007; Sicardy et al., 2003) and perhaps Triton (Elliot et al., 2000). Remembering also that pressure levels detected during refractive occultations are inversely proportional to distances, and considering that better signal to noise ratios than obtained in this work can be reached, it appears that atmospheres at the nanobar level can be

detected for trans-neptunian objects, using the method described in this paper.

7. Conclusions

The 8 September 2001 stellar occultation by Titania provides a newly determined radius for Titania, $R_T = 788.4 \pm 0.6$ km (1-σ error bar), in agreement with the *Voyager* limb image retrieval which gave $R_T = 788.9 \pm 1.8$ km (Thomas, 1988). Our value, combined to the mass $GM = 2.343 \times 10^{11}$ m^3 s^{-2} given by Taylor (1998), yields a density of $\rho = 1.711 \pm 0.005$ g cm^{-3}. This represents a silicate to ice ratio of $\sim$0.5 (Brown et al., 1991), a much higher silicate fraction than the satellites of Saturn, in agreement with the observed relative depletion of surface ice in the uranian system. No oblateness is detected, down to a limit of $r_{eq} - r_{po} = -1.3 \pm 2.1$ km for the difference between equatorial and polar radii, again in agreement with *Voyager* results. Our measurements demonstrate the capabilities of stellar occultations to retrieve kilometric or better accuracies for the size of objects in the outer Solar System.

HIP 106829 angular diameter is derived: 0.54 ± 0.03 mas, corresponding to 9.8 ± 0.2 solar radii, typical of a K0 III giant star.

The offset of Titania with respect to the DE405 + URA027 (GUST86 theory) is found to be $\Delta\alpha_T \cos(\delta_T) = -108 \pm 13$ mas and $\Delta\delta_T = -62 \pm 7$ mas, in the ICRF J2000.0 reference frame on Sept. 8, 2001, 2:00 UT. This is mainly attributable to an offset in Uranus barycentric ephemeris, that we estimate to $\Delta\alpha_U \cos(\delta_U) = -100 \pm 25$ mas and $\Delta\delta_U = -85 \pm 25$ mas. Another Titania occultation observed on August 1st, 2003, confirms this finding, as it yields an offet of $\Delta\alpha_T \cos(\delta_T) = -127 \pm 20$ mas and $\Delta\delta_T = -97 \pm 13$ for the satellite.

Our analysis allows to set upper limits to an atmosphere for Titania, at the level of 10–20 nbar for CO_2, CH_4 or N_2 atmospheres. Although an atmosphere around Titania was not expected, this is 3 orders of magnitude less than the currently observed pressures on Pluto and Triton. As pressure levels detected during refractive occultations are inversely proportional to distances, the upper limits obtained on Titania open promising perspectives to constrain atmospheres of trans-neptunian objects at a few nanobars level, as developed in this paper.

References

Allen, C.W., 1976. Astrophysical Quantities, third ed.. Athlone, London, p. 209.

Arlot, J.-E., Dourneau, G., Le Campion, J.F., 2008. An analysis of Bordeaux meridian transit circle observations of planets and satellites (1997–2007). Astron. Astrophys. 484, 869–877.

Brown Jr., G.N., Ziegler, W.T., 1980. Vapor pressure and heats of vaporization and sublimation of liquids and solids of interest in cryogenics below 1-atm pressure. Adv. Cryogen. Eng. 25, 662–670.

Brown, R.H., Cruikshank, D.P., Morrison, D., 1982. Diameters and albedos of satellites of Uranus. Nature 300, 423–425.

Brown, R.H., Johnson, T.V., Synnott, S., Anderson, J.D., Jacobson, R.A., Dermott, S.F., Thomas, P.C., 1991. Physical properties of the uranian satellites. In: Bergstrahl, Miner, Matthews (Eds.), Uranus. Univ. of Arizona Press, Tucson, pp. 513–527.

Buratti, B., Wong, F., Mosher, J., 1990. Surface properties and photometry of the uranian satellites. Icarus 84, 203–214.

Claret, A., 2000. A new non-linear limb-darkening law for LTE stellar atmosphere models: Calculations for $-5.0 < \log[M/H] < +1$, 2000 K $< T_{eff} < 50000$ K, at several surface gravities. Astron. Astrophys. 363, 1081.

Croft, S.K., Soderblom, L.A., 1991. Geology of the uranian satellites. In: Bergstrahl, Miner, Matthews (Eds.), Uranus. Univ. of Arizona Press, Tucson, pp. 561–628.

Dumas, C., Merlin, F., Barucci, M.A., de Bergh, C., Hainault, O., Guilbert, A., Vernazza, P., Doressoundiram, A., 2007. Surface composition of the largest dwarf planet 136199 Eris (2003 UB_{313}). Astron. Astrophys. 471, 331–334.

Elliot, J.L., and 17 colleagues, 2000. The prediction and observation of the 1997 July 18 stellar occultation by Triton: More evidence for distortion and increasing pressure in Triton's atmosphere. Icarus 148, 347–369.

Elliot, J.L., and 28 colleagues, 2003. The recent expansion of Pluto's atmosphere. Nature 424, 165–168.

Elliot, J.L., Person, M.J., Gulbis, A.A.S., Souza, S.P., Adams, E.R., Babcock, B.A., Gangestad, J.W., Jaskot, A.E., Kramer, E.A., Pasachoff, J.M., Pike, R.E., Zuluaga, C.A., Bosh, A.S., Dieters, S.W., Francis, P.J., Giles, A.B., Greenhill, J.G., Lade, B., Lucas, R., Ramm, D.J., 2007. Changes in Pluto's atmosphere: 1988–2006. Astron. J. 134, 1–13.

Fienga, A., Manche, H., Laskar, J., Gastineau, M., 2008. INPOP06: A new numerical planetary ephemeris. Astron. Astrophys. 477, 315–327.

Giorgini, J.D., Yeomans, D.K., Chamberlin, A.B., Chodas, P.W., Jacobson, R.A., Keesey, M.S., Lieske, J.H., Ostro, S.J., Standish, E.M., Wimberly, R.N., 1996. JPL HORIZONS on-line Solar System data and Ephemeris computation service. Bull. Am. Astron. Soc. 28 (3), 1158. JPL/Horizons website as of Jul. 1, 2008: http://ssd.jpl.nasa.gov/horizons.html.

Grundy, W.M., et al., 1999. Near-infrared spectra of icy outer Solar System surfaces: Remote determination of H_2O ice temperatures. Icarus 142, 536–549.

Grundy, W.M., Young, L.A., Spencer, J.R., Johnson, R.E., Young, E.F., Buie, M.W., 2006. Distributions of H_2O and CO_2 ices on Ariel, Umbriel, Titania, and Oberon from IRTF/SpeX observations. Icarus 184, 543–555.

Hanel, R., Conrath, B., Flasar, F.M., Kunde, V., Maguire, W., Pearl, J., Pirraglia, J., Samuelson, R., Cruikshank, D., Gautier, D., Gierasch, P., Horn, L., Schulte, P., 1986. Infrared observations of the uranian system. Science 233, 70–74.

Hansen, C.J., Esposito, L., Stewart, A.I.F., Colwell, J., Hendrix, A., Pryor, W., Shemansky, D., West, R., 2006. Enceladus' water vapor plume. Science 311, 1422–1425.

Helfenstein, P., Ververka, J., Thomas, P.C., 1988. Uranus satellites—Hapke parameters from Voyager disk-integrated photometry. Icarus 74, 231–239.

Jacobson, R.A., Campbell, J.K., Taylor, A.H., Synnott, S.P., 1992. The masses of Uranus and its major satellites from Voyager tracking data and Earth-based uranian satellite data. Astron. J. 103, 2068–2078.

Jewitt, D.C., Luu, J., 2004. Crystalline water ice on the Kuiper belt object (50000) Quaoar. Nature 432, 731–733.

Lainey, V., 2008. A new dynamical model for the uranian satellites. Planet. Space Sci. 56, 1766–1772.

Laskar, J., Jacobson, R.A., 1987. GUST86—An analytical ephemeris of the uranian satellites. Astron. Astrophys. 188, 212–224.

Licandro, J., di Fabrizio, L., Pinilla-Alonso, N., de Leon, J., Oliva, E., 2006a. The methane ice rich surface of large TNO 2005 FY_9: A Pluto-twin in the trans-neptunian belt? Astron. Astrophys. 445, L35–L38.

Licandro, J., Grundy, W.M., Pinilla-Alonso, N., Leisy, P., 2006b. Visible spectroscopy of 2003 UB_{313}: Evidence for N_2 ice on the surface of the largest TNO? Astron. Astrophys. 458, L5–L8.

Matsuda, K., 1996. Time keeping office and NTP servers. Astron. Her. 89, 210–215. Network Time Protocol website as of Jul. 1, 2008: http://www.ntp.org.

Murray, C.D., Dermott, S.F., 1999. Solar System Dynamics. Cambridge University Press, Cambridge, UK.

Ochsenbein, F., Bauer, P., Marcout, J., 2000. Astron. Astrophys. 143, 221. Vizier website as of Jul. 1, 2008: http://vizier.u-strasbg.fr.

Perryman, M.A.C., et al., 1997. The Hipparcos catalogue. Astron. Astrophys. 323, 49–52.

Porco, C.C., and 24 colleagues, 2006. Cassini observes the active south pole of Enceladus. Science 311, 1393.

Press, W.H., Flannery, B.P., Teukolsky, S.A., Vetterling, W.T., 1986. Numerical Recipes. Cambridge University Press, Cambridge, UK.

Roques, F., Moncuquet, M., Sicardy, B., 1987. Stellar occultations by small bodies: Diffraction effects. Astron. J. 93, 1549–1558.

Schaller, E.L., Brown, M.E., 2007a. Volatile loss and retention on Kuiper belt objects. Astron. Astrophys. 659, 61–64.

Schaller, E.L., Brown, M.E., 2007b. Detection of methane on Kuiper belt object (50000) Quaoar. Astrophys. J. 670, 49–51.

Sicardy, B., and 40 colleagues, 2003. Large changes in Pluto's atmosphere as revealed by recent stellar occultations. Nature 424, 168–170.

Sicardy, B., and 51 colleagues, 2006. The two Titan stellar occultations of 14 November 2003. J. Geophys. Res. 111 (E11). E11S91.

Taylor, D.B., 1998. Ephemerides of the five major uranian satellites by numerical integration. Astron. Astrophys. 330, 362–374.

Thomas, P.C., 1988. Radii, shapes, and topography of the satellites of Uranus from limb coordinates. Icarus 73, 427–441.

van Belle, G.T., 1999. Predicting stellar angular sizes. Publ. Astron. Soc. Pacific 111, 1515–1523.

Waite, J.H., and 13 colleagues, 2006. Cassini ion and neutral mass spectrometer: Enceladus plume composition and structure. Science 311, 1419–1422.

Washburn, E.W., 1930. International Critical Tables of Numerical Data: Physics, Chemistry and Technology, vol. 7. McGraw-Hill, New York, p. 11.

Wenger, M., Ochsenbein, F., Egret, D., Dubois, P., Bonnarel, F., Borde, S., Genova, F., Jasniewicz, G., Laloë, S., Lesteven, S., Monier, R., 2000. The SIMBAD astronomical database. The CDS reference database for astronomical objects. Aston. Astrophys. 143, 9–22. Simbad website as of Jul. 1, 2008: http://simbad.u-strasbg.fr.

Zahnle, K., Schenk, P., Levison, H., Dones, L., 2003. Cratering rates in the outer Solar System. Icarus 163, 263–289.